Title	Study on Young Debris Disk around HD 141569 A with Hubble Space Telescope
Author(s)	小西, 美穂子
Citation	大阪大学, 2016, 博士論文
Version Type	VoR
URL	https://doi.org/10.18910/56082
rights	
Note	

Study on Young Debris Disk around HD 141569 A with *Hubble Space Telescope*

ハッブル宇宙望遠鏡を用いた
HD 141569 A周囲にある若い残骸円盤の研究

Mihoko KONISHI

February 2, 2016

A Dissertation for the Degree of Doctor of Philosophy

Department of Earth and Space Science,
Graduate School of Science, Osaka University

Abstract

Planets are considered to form in protoplanetary disks during the star formation process. Protoplnetary disks and planets interact with each other. Thus, detail understanding of the disk structures is important in order to elucidate star and plant evolution. Protoplanetary disks have been imaged recently, and it has become clear that these disks have complex structures. Deailed investigation of these structures will facilitate understanding of planet formation.

This work is focused on a disk around HD 141569 A (spectral type: B9.5, age: 5 Myr). This is a young debris disk, containing various complex structures. Specifically, optical and near-infrared observations have revealed two rings, known as the inner and the outer rings, as well as spiral structures, and have also revealed that the area inside the inner ring is a cavity (<175 AU). In addition, emission from dust and CO gas has been detected inside the inner ring using mid-infrared and radio emission lines. In this work, data obtained by Space Telescope Imaging Spectrograph (STIS) as part of the *Hubble Space Telescope* (HST) general observer program are analyzed by dividing the scattered light from the disk and star. As a result, the scattered light from an inner disk component within the known inner ring is detected for the fist time. The inner disk component extends from 45 to 120 AU in deprojected stellocentric distance, with no gaps or a cavity. A spiral is observed at 130 AU. A pericenter offset of 6 AU may exist towards the north. Further, the inner disk component has surface brightness asymmetry. An unseen planet would trigger structures such as the spiral and the gap between the inner disk component and the inner ring. However, our data indicate that there is no point source heavier than 9 M_J in the gap. On the other hand, the mass of the planet that could create such a gap is <1 M_J, as estimated by the dynamical model. Thus, we cannot reject the possibility that an unseen planet creates the gap. It is, however, reasonable that the

discovered spiral is excited by an unseen planet, although the gap may be formed by disk instability.

This work reveals that the protoplanetary disk around HD 141569 A has complex structures that cannot be explained by the known model. Therefore, it is necessary to develop a full picture of star and planet formation, including their interaction, using both high-contrast observations and exact modeling.

Contents

List of Figures

List of Tables

Chapter 1

Circumstellar Disk Evolution and Plant Formation

Core accretion model (e.g., Hayashi et al., 1985) was built up to explain the Solar System formation. It well represents planet architectures in the Solar System. This model is, however, insufficient to explained exoplanets which have different property from the Solar System planets, such as Hot Jupiters, high eccentric planets, and a few Jupiter-mass planets distant from the star ($\sim$100 AU). In order to interpret the formation of such planets, various ideas were introduced (e.g., gravitational instability, planet migration, and planet scattering). Circumstellar disks and planets are supposed to co-evolve as interact each other. Therefore, understanding disk structures and properties is necessary so as to elucidate the uniform planet formation.

1.1 Star and Circumstellar Disk Formation

Stars are formed within a molecular cloud in a star formation region. First, the molecular cloud gravitationally collapses and, protostar cores are formed. The protostars increase in size by acquiring gas supplied by circumstellar disks called as protoplanetary disks. The protoplanetary disks are composed of dust and gas that cannot accrete directly onto the stars because of their angular momenta. Note that some jet features from the star can be detected at this stage (e.g., HH 30; Burrows et al., 1996), and phenomena reduce the overall angular momentum of the system. Protoplanetary disks surrounding pre-main-sequence stars are gas-rich and optically thick; thus, they are opaque. As time passes, the materials in the disk begin to clear, beginning at the area close to the primary star (e.g., Brown et al., 2007). Various mechanisms can explain this clearing, such as grain growth (e.g., Dullemond & Dominik, 2005), photo evaporation (e.g., Alexander et al., 2006), close binary perturbation (e.g., Ireland & Kraus, 2008), and planet-disk interaction (e.g., Lubow & D'Angelo, 2006). When the gas disappears, the central stars become main-sequence stars. Most stars have remnant disks that include various size of the dust and small amount of gas (i.e., they are optically thin). Star and planet systems are born in this way. Protoplanets form within the disk through the assembly of grown planetesimals and gas, which is why the term "protoplanetary disks" is used.

Stars with protoplanetary disks exhibit an infrared excess in their spectral energy distributions (SED). In the case of a star with a continuous disk, such as an early-stage protoplanetary disk, the dust in the disk absorbs the light from the star and emits it as infrared light. This generates an excess in SED in the near to far infrared ranges (wavelength of a few to hundreds microns). The disk states are referred to as primordial, transitional, and debris disk. Disks classified as primordial disks have large infrared excesses and large amount of gas. The gas-to-dust mass ratios are generally similar to those of interstellar clouds (100:1) (e.g., Knapp & Kerr, 1974). Star and planet formation is ongoing inside primordial disks; however, this behavior cannot be observed because the disks are optically thick. Transitional disks,

which are considered to be the next developmental stage after the primordial disks, have a deficit in the infrared excess of $<\sim 10$ μm (e.g., Strom et al., 1989). This is caused by an absence or shortage of hot and small dust grains in the innermost area close to the star. Conversely, mid- and far-infrared excess remains apparent in the SED, which indicates that the dust constituting the outer disk remains in place, and that the disk is optically thick. Transitional disks usually exhibit CO emission, similar to primordial disks (e.g., Qi et al., 2004), which indicates that their outer disks still contain a large amount of gas. Transitional disks are considered to be the evolutionary phase between primordial disks to the next stage (debris disk), because they are share common features with both of these disk types.

Debris disks are found around stars aged between 10 Myr and 10 Gyr. The infrared excess in the SED is low (L_{disk}/L_{star} $<\sim$ 10^{-3}), which indicates a low dust mass surrounding the star. Debris disks also have less or no gas than the earlier stages. Some exhibit localized gas emissions (e.g., β Pic; Dent et al., 2014 and Oph IRS 48; van der Marel et al., 2015), whereas others have centrally concentrated gas and millimeter-sized debris (e.g., HD 21997; Moór et al., 2013). Debris disks typically have ring-like structures with narrow width (e.g., HR 4796; Schneider et al., 1999). Large extended and faint structures can bee observed in some debris systems (Schneider et al., 2014), which are sometimes truncated by companions in the system. Debris disks surrounding old stars (>1 Gyr) have been found. Thus, the debris is considered to be produced by planetesimals collisions, because small dust grains are rapidly expelled and, therefore, are not present in.

Figure 1.1 summarizes the whole view of star and disk formation described above. Empirically, low-mass stars are classified into four types: Class 0, I, II, III, based on the SED slope. Two different classification systems cannot have a one-to-one correspondence. However, Class II and Class III are considered to be roughly equivalent to primordial disk and debris disk, respectively.
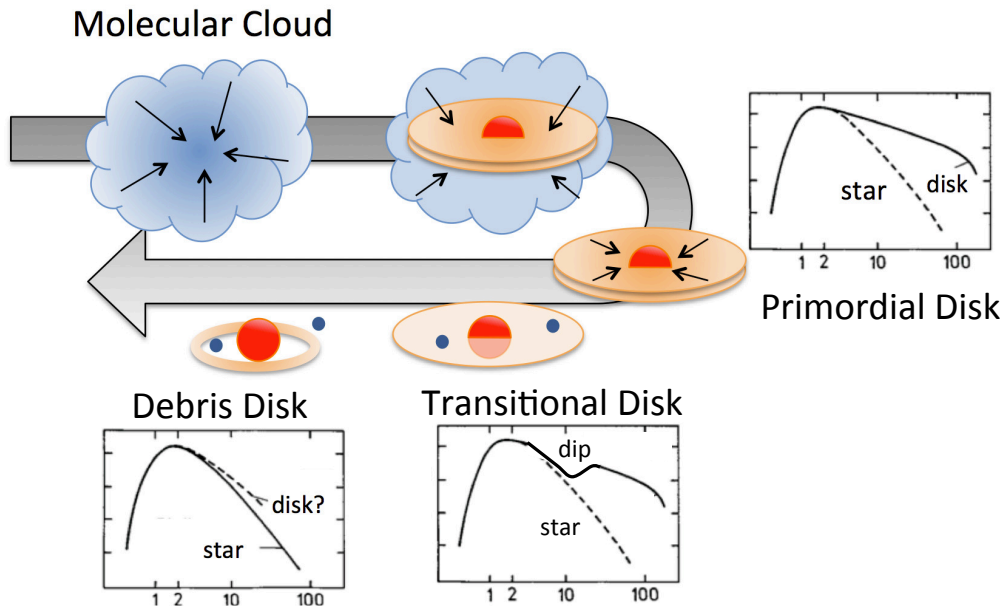
Figure 1.1: Sketch of star and disk formation (made in reference to Figure 11 of Bachiller, 1996). Typical SED cartoons of primordial, transitional, and debris disks are also shown.

1.2 Disk Compositions

This section is summary of protoplanetary disk compositions, in reference to two review papers (Williams & Cieza, 2011; Andrews, 2015).

1.2.1 Dust

We can observe thermal emission and scattered light from the dust. Thermal emission from the various-temperature dust contributes to a wide wavelength range of the infrared excess. When we assume the toy model (negligible scattering, vertically thin, and thermodynamic equilibrium), optically thick emission are given from the $\tau=1$ layer (τ; opacity), like a thermometer. On the other hand, optically thin emission has the information of temperature, column density, and opacity. The thermal emission is useful to estimate the dust disk mass. Figure 1.2 shows where the typical dust emission (from mid-infrared to submillimeter) comes from in case of GO Tau (Andrews, 2015). Form the Figure 1.2, detecting the 4.5 μm emission indicates observing the

4

Figure 1.2: (Left) The SED of GO Tau. Black dots are observed results. Gray line shows the models of the stellar photosphere. Blue line is an dust disk computed for s simple parametric structure. Red line is the mid-infrared spectrum taken by *Spitzer*. (Right) Two-dimensional map of the regions that emit 80% of the flux (4.5 μm, 24 μm, 70 μm, and 1.3 mm). They are taken from Andrews (2015), and more details are written in it.

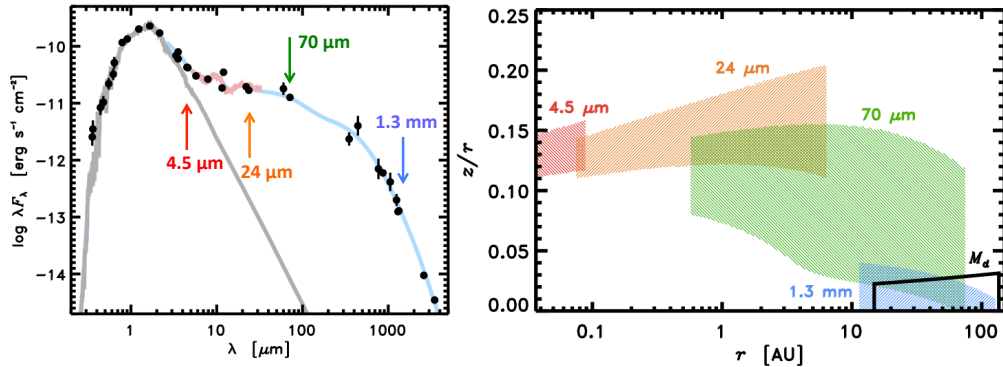innermost region (<0.1 AU), but only the upper layer of the disk. The mid-plane dust distribution can be observed by using the 1.3 mm emission (<10 AU). Considered the typical disk distance of 100 AU, the thermal emission is comes from the region of $<<0''1$, which is near or under the diffraction limit of the current telescopes. Interferometric measurements are, therefore, useful to estimate the dust mass.

On the other hand, scattered light is observed in the disk surface layer. It also can be detected over a large range of densities. The scattering is efficient when the using wavelength is similar to the dust size (~ 1 μm). Observational techniques in the near-infrared are well developed, and can detect substructures of ~ 10 AU scales. Therefore, the scattered light is a probe to expose the disk structures (e.g., inclination). Also, the dust polarization indicates the dust natures (e.g., sizes and compositions).

Dust nature changes as time go on, such as location in the disk and size. The dust grows up by coagulation and becomes planetesimals. There is a observational problem at this stage. It is hard to detect large grains because of the sensitivity and its low density, although it occupies a large amount of disk dust mass. It is an obstacle to estimate the precious disk mass. As the dust evolves, it concentrates on the mid-plane. It also moves inward by

accretion and outward by diffusion, since the small-grain dust is well coupled with the gas. Therefore, the dust distribution is one of the keys to interpret the disk evolution.

1.2.2 Gas

Gas occupies 99% of the total mass of the interstellar medium (ISM). Protoplanetary disks are created by ISM, and thus the gas-to-dust ratio is considered to 100:1 as similar to that of ISM. The fact was reported in some disks (e.g., AB Aur; Piétu et al., 2005), however, the measurement accuracy is needed because the gas deplete as its evolution. The disk gas contains a significant portion of H_2, but the H_2 gas is hard to detect because it has no electric dipole. Thus, the CO gas is the best observer of the disk gas. There are many observations held by using CO lines of rotation and vibration transitions (e.g., Goto et al., 2006; Flaherty et al., 2016). Various kinds of CO observation (including isotopes) indicate the vertical temperature gradient as well as the radial one. It would affect the dust nature and also the planet formation.

Finally, we note the vertical structures of the protoplanetary disks. The disks are in vertical hydrostatic equilibrium when assumed the dust follows the same distribution. When the equation is solved, the scale height is proportional to temperature and distance from the star ($H \propto T \times r^3$). The surface layer is irradiated by the star, and it becomes hot. Therefore the scale height is larger as temperature and distance are larger. This effect derives the "flared" disks. Most protoplanetary disks have the flared shape as observed by using scattered light (e.g., HH 30; Burrows et al., 1996).

1.3 Disk-planet Interactions

The uniform disk architectures are described in the previous section. Disks may be seemed to be flat and featureless. However, recent observations discovered various kinds of disk structures, such as gaps, spirals, cavities/holes, and asymmetry (e.g., truncations, pericenter offsets, and surface brightness

asymmetries). What are the origins of these structures? A lot of researchers are making attempts to explain such structures in terms of modeling and observations. The most promising origin is that forming planets create structures by interacting with dust and gas in the disks. Herein, the previous studies are summarized, and also what we understand or not is made clear. Note that the current observation technique does not reach the sensitivity to detect planets embedded in the disk.

Gaps

As a giant planet grows up, its gravity at the planet position is larger. Due to the planet gravity itself, gas is scattered at the planet position. This makes the gas density low, and creates annulus-shape low density area called as "gap". The gaps formation has been investigated by many researchers (e.g., Kanagawa et al., 2015b and see also their citations). The gap structures were found in the real protoplanetary disks, thanks to the recent progress in the observational techniques (e.g., HD 169142; Momose et al., 2015 and HL Tau; ALMA Partnership et al., 2015), which shown in Figure 1.3. Kanagawa et al. (2015a) obtained the relationship between the embedded planet mass, the gap depth, disk temperature and disk viscosity. They also mentioned that the observed gaps of HD 169142 (50 AU) and HL Tau (30 AU) would be opened by the planets of >0.4 M$_J$ and >0.3 M$_J$, respectively. The model estimations, however, have uncertainty because the disk properties are unclear (e.g., viscous parameter (α) and disk temperature). In addition, we do not understand the amount of gas in the the individual disk, which would invoke the difference of gap forming timescale (also including no gap structures).

Cavities or Holes

If the gap opened near the star, the inner-side disk would disappear, and void area is made. The planet accrete a large amount of the disk material around it, if the formed planet is massive. This would cause decreasing of the supply of the disk interior to the gap. Thereby, the inner most region
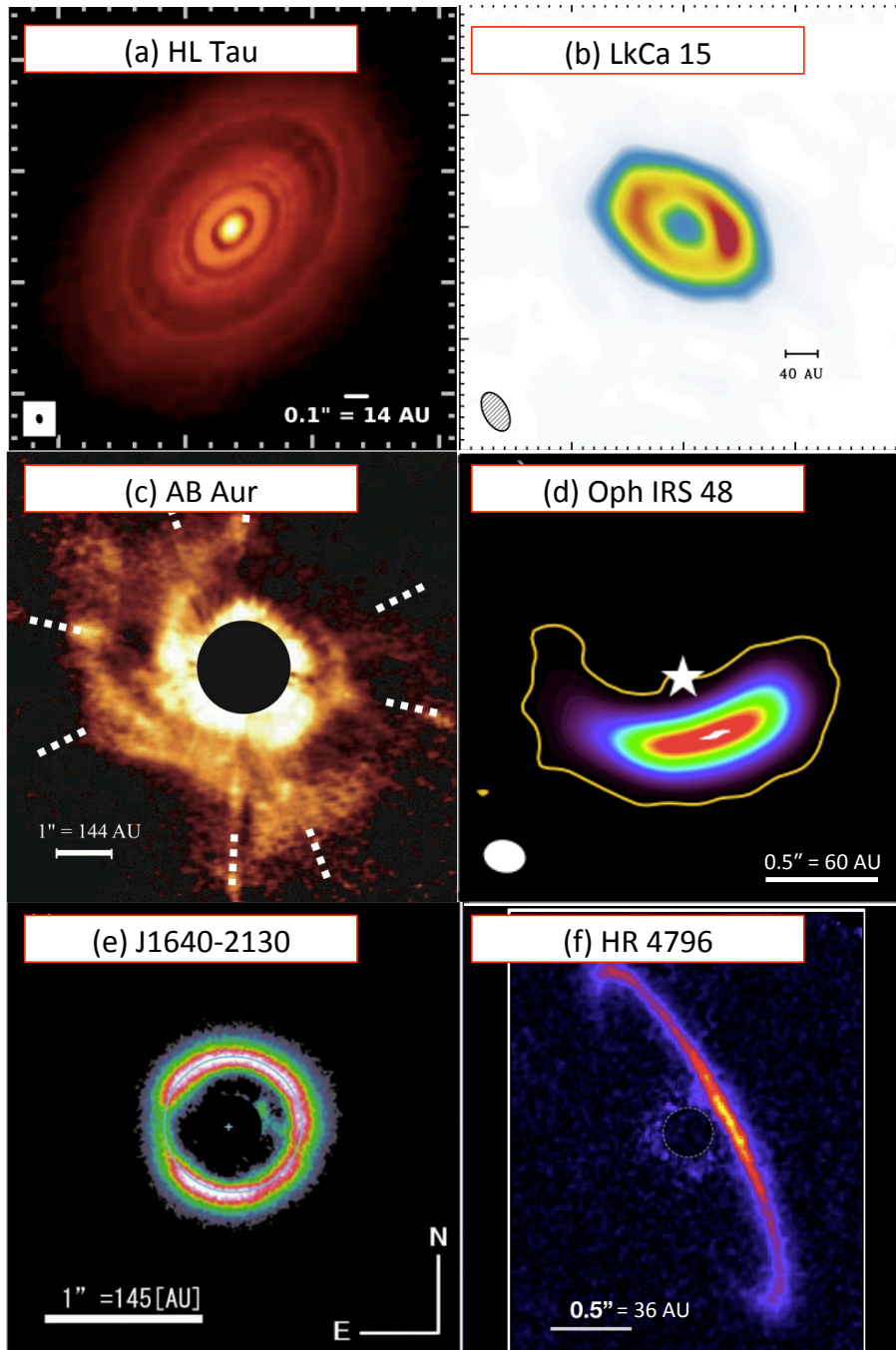
Figure 1.3: Diversity of disk structures obtained to date. (a) Many gap structures in HL Tau disk observed by ALMA (ALMA Partnership et al., 2015) in 1.0 mm continuum. (b) 870 μm continuum emission from LkCa 15 transitional disk obtained by PdBI and SMA, which shows a large cavity. (c) H-band scattered disk of AB Aur obtained by Subaru Telescope (Fukagawa et al., 2004). Spiral structures can be seen in the disk. (d) 680 GHz image of Oph IRS 48 taken by ALMA (van der Marel et al., 2015). Strong brightness asymmetry can be seen. (e) Polarized intensity image of 2MASS J16042165-2130284 obtained by Subaru Telescope (Mayama et al., 2012). There is a arc in the gap. (f) Ring-like structure around HR 4796 using GPI by detecting H-band polarized intensity (Perrin et al., 2015). Note that some indicators were added.

shows no dust and gas features, which called as "cavity" or "inner hole" (see citations in Andrews, 2015). The cavity structures are reported in the transitional disks. Figure 1.3 (b) shows 870 μm continuum emission from the LkCa 15 transitional disk obtained by Plateau de Bure interferometer (PdBI) and Submillimeter Array (SMA). There are a large cavity inside 40–50 AU seen in the image. A deficit of the dust continuum at the inner most region means small amount of hot dust exits near the star. This produces a dip at $\sim$10 μm in the SED, as introduced in Section 1.1. This is why cavity structures can be seen in various transitional disks (e.g., SR 21, LkHα 330, and HD 135344 B reported by Brown et al., 2009).

There are an alternative explanation to create a cavity. This is introduced in the Section 1.3.1.

Spiral Structures

Figure 1.3 (c) shows some spiral structures in AB Aur disk (Fukagawa et al., 2004), and some protoplanetary disks are reported to have spiral structures (e.g., SAO 206462; Muto et al., 2012, MWC 758; Benisty et al., 2015, and HD 100453; Wagner et al., 2015). Muto et al. (2012) proposed the density wave theory to interpret the spiral structures seen in SAO 206462, and obtained reasonable results. Dong et al. (2015) studied the density wave induced by giant planets, using 3D global hydro simulations coupled with radiative transfer calculation. They found that a giant planet can produce detectable spiral arms both interior and exterior to the planet orbit. In addition, two inner spirals are well representative to observational result both of SAO 206462 and MWC 758. Therefore, it is reasonable that spiral structures are caused by the forming plaenets.

Binaries, more massive than planets, also produce spirals. Dong et al. (2016) used the similar model described above (Dong et al., 2015) to probe that spirals of HD 100453 caused by its companion. The companion has already reported to be co-moving M dwarfs at the projected separation of 120 AU (Wagner et al., 2015 and see also their citations). Their simulation could produce the similar features of HD 100453, such as two spirals and

disk truncation. There is, thus, a possibility that spirals are excited by the companions massive than planets.

The density wave model can produce various patterns of spiral, by changing the planet mass, location, and disk parameter (e.g., disk viscosity). We cannot confirm the origin of spiral structures unless detecting perturbations. However, it is impossible to detect such planets with the current imaging technique (e.g., planets are not detected in SAO 206462 and MWC 758 systems as described above). Note that the gravitational instability could be also produce spiral structures (e.g.,Nelson et al., 1998).

Asymmetry

Some asymmetry feature are reported in the disks, such as truncation, surface brightness asymmetry, and pericenter offsets. There are dynamical interactions in the multiple systems. Stellar mass objects in the systems strongly affect disk structures. Many models indicate that the disks are truncated by the tidal force at about one-third of the semi-major axis (e.g., Artymowicz & Lubow, 1994). For example, HD 100453 disk are truncated at ∼45 AU, which might be excited by the companion (Wagner et al., 2015). Figure 1.3 (d) are 680 GHz (440 μm) image of Oph IRS 48 obtained by Atacama Large Millimeter/submillimeter Array (ALMA) (van der Marel et al., 2015). This image shows the strong brightness asymmetry. This is considered to concentrate the large debris in the south area; this feature is called as "dust trap". This may have a relation with the planet formation. Figure 1.3 (e) shows another asymmetric structure in the gap, as well as brightness asymmetry. Mayama et al. (2012) observed 2MASS J16042165-213028, and detected a arc in the gap. This structure is also considered to be excited by an unseen bodies.

The above asymmetries are related with dust as well as planets. Herein, a example of other phenomena is introduced. When the flared disk is irradiated by the primary star, the upper layer of the disk becomes hot. The scale height of the disk is higher as the temperature is larger. This instability is introduced by Watanabe & Lin (2008) as "thermal wave". This would cause brightness or structure asymmetries.

1.3.1 Transitional Disk

At the stage of transitional disks, the disk densities are depleted such as by turbulent transport (e.g., Shakura & Sunyaev, 1973) and by magnetic winds (e.g., Blandford & Payne, 1982). This process takes some times (tens of Myr; Andrews, 2015) until the disk faded away, but there is additional quick mechanism "photoevapolation" (e.g., Clarke et al., 2001). High-energy radiation (e.g., X-ray) attacks on the gas in the disk, and the gap is created at a few AU (e.g., Liffman, 2003). The inner disk will quickly accrete onto the star ($\sim$0.1 Myr; e.g., Alexander et al., 2006), and the cavity is created. This is another mechanism that the observed cavities (e.g., Figure 1.3 (b)) are explained.

1.3.2 Debris Disk Architecture

Debris disks typically have narrow ring structures, such as HR 4796 A ring (Figure 1.3 (f). The rings are convenient for precious measurement of the geometry. Thanks to the high-resolution observations, the presence of pericenter offsets are found (e.g., HR 4796; Schneider et al., 2009). The primary star does not locate at the ring center, which indicates that there are other perturbations exited the offsets.

One of the interesting features in debris disk is stirring. There are many perturbation sources, since dust in the debris disk sufficiently grows up. The large dust as well as planet bodies stirs the disk, which cause the brightness differences as a function of age (about more detail, see Wyatt, 2008). The disk brightness is, therefore, considered to be more complected.

1.4 Exoplanets

Apart from disk observations, exoplanets have been successfully detected using a variety of techniques. The number of confirmed exoplanets has recently exceeded two thousand. Herein, the exoplanet hunting methods and examples of imaged exoplanets are reviewed. Note that direct imaging observations are necessary to discuss the disk-planet interaction. However, the

sensitivity of imaging reaches to detect only a few Jupiter-mass planets.

1.4.1 Exoplanet Hunting

The First exoplanet, 51 Peg b, was discovered via radial velocity variations (Mayor & Queloz, 1995). 51 Peg b has anomalous features that are different from those of the planets in the Solar System. Its mass is $> \sim 0.5$ M_J and its semi-major axis is ~ 0.5 AU, i.e., it is a typical Hot Jupiter. Radial velocity observations indicate that the planet mass (M_{planet}) has degenerated as result of inclination i ($M_{planet} \sin i$). If the i of the system is known, M_{planet} can be obtained. Transit observations provide information on i, because flux dimming is only obtained in the case of a close edge-on system. This techniques provide radial information for planets, and, thus, we can estimate planet densities by combining transit observations with the results of radial velocity observations. Information on the density is important for determining the exoplanet composition (e.g., Nettelmann et al., 2011). However, these two techniques have a bias, as heavy, big, and close exoplanets are easily detected. On the other hand, exoplanets detected with microlensing are close to the system snowline and have M_{planet} values as low as Earth–Neptune size. Microlensing events are very rear; however, this approach is unique in that free-floating planets can be found, because there is no bias in terms of the target brightness and distance from the Sun (e.g., Sumi et al., 2011).

1.4.2 Imaging Exoplanets

The exoplanet imaging technique directly detects thermal emission from exoplanets far from the primary star (tens to hundreds of AU). Imaging is challenging, because the primary star is significantly brighter than exoplanets, and, therefore, the number of confirmed exoplanets is small. The use of spectrograph to characterize exoplanets is promising, as the projected positions of these planets can be obtained. It is helpful to discuss the relationships between the exoplanets and protoplanetary disk structures. Below, the well-known exoplanets are discussed.

Figure 1.4 shows the three exoplanetary system (HR 8799; Marois et al., 2010, β Pic; Macintosh et al., 2014, GJ 504; Kuzuhara et al., 2013). HR 8799 is the most well-know star as only multi-planet system that has been detected via imaging (Marois et al., 2008, 2010). The system contains four Jovian mass planets (b: $\sim$7, c: $\sim$10, d: $\sim$10, and e: $\sim$9 M_J), with projected separations of $\sim$70, $\sim$40, $\sim$25, $\sim$15 AU, respectively. For these planets, various characteristics are reported and discussed. One of the most interesting results is the planet spectroscopy. The spectra of HD 8799 b and c have been recorded by the Palomar 5m Hale Telescope, and atmospheres have also been examined (Oppenheimer et al., 2013). Recently, Gemini Planet Imager (GPI) and Spectro-Polarimetric High-contrast Exoplanet REsearch (SPHERE) on Very Large Telescope (VLT) have provided further details on the natures of these planets (Ingraham et al., 2014; Zurlo et al., 2015; Bonnefoy et al., 2015).

β Pic b has a mass of $\sim$7 M_J, with a projected separation of $\sim$9 AU. A large debris disk has been imaged (e.g., Golimowski et al., 2006). Snellen et al. (2014) measured a spin velocity of 25 km s^{-1} for β Pic b, and revealed that it spins significantly faster than any planets in the Solar System; these results are in line with the extrapolation of the known spin velocity trend with regard to planet mass.

GJ 504 b was discovered by Subaru Telescope, and has a mass of $\sim$4 M_J and a projected distance of $\sim$45 AU (Kuzuhara et al., 2013). This exoplanet has the lowest temperature among the exoplanets discovered via imaging to date. Its temperature is estimated to be similar to that of T dwarfs and, thus, it is the only exoplanet that exhibits CH_4 absorption (Janson et al., 2013a). A recent study has measured its properties in detail (e.g., its temperature, metallicity, and cloud opacity) via spectral fitting, and noted that GJ 504 b was formed like a planet, rather than a binary companion (Skemer et al., 2015).

1.5   Open Questions and the Goal

How do the forming planets interact with protoplanetary disks? What structures and physical quantity are the evidence of planets? How do we distin-

(a) HR 8799

(b) β Pic
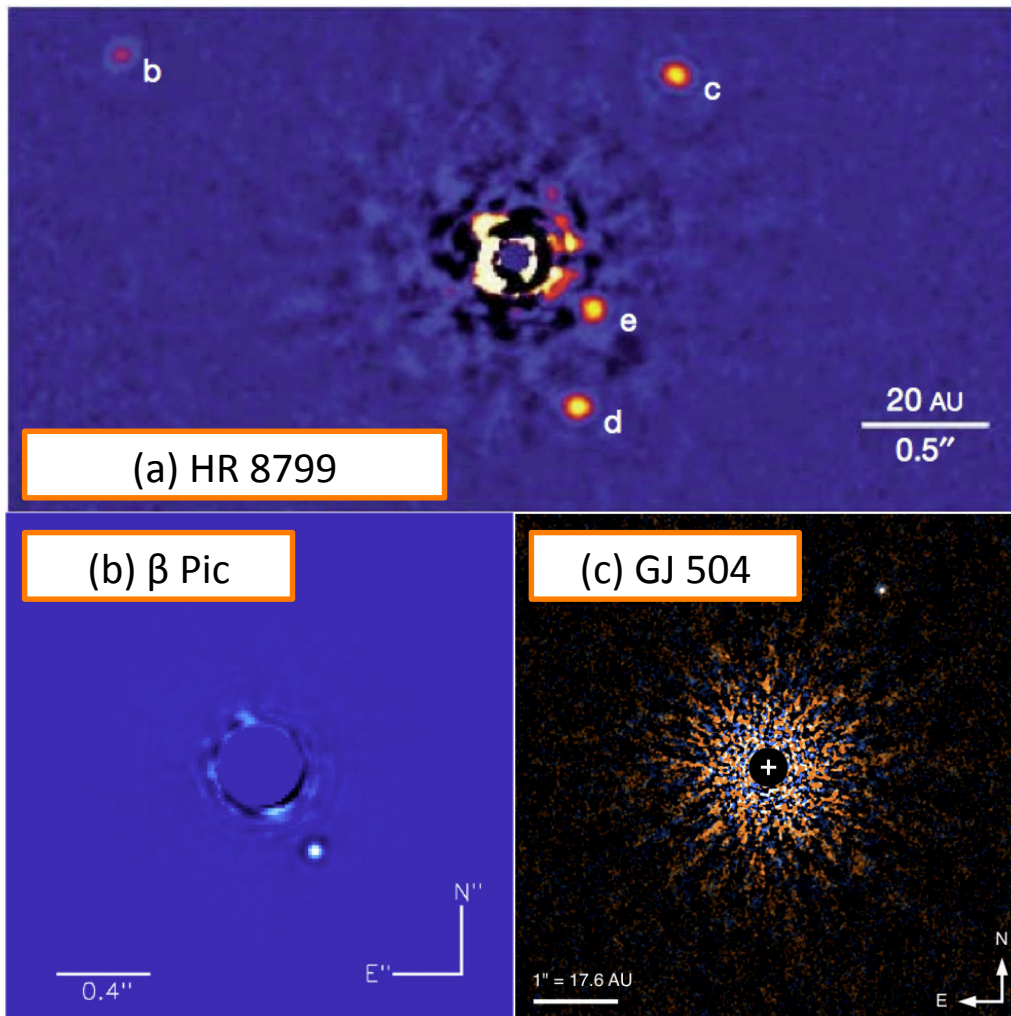
(c) GJ 504

20 AU

0.5″

0.4″

N″

E″

1″ = 17.6 AU

N

E

Figure 1.4: Examples of the imaged exoplanets. (a) HR 8799 b, c, d, and e obtained by Keck Telescope in the L' band (Marois et al., 2010). (b) β Pic b obtained by GPI in 1.5–1.8 μm (Macintosh et al., 2014). (c) GJ 504 b obtained by Subaru Telescope in the H band (Kuzuhara et al., 2013).

guish between features exited by planets and other phenomena? We have obtained many observational results of protoplanetary disks. In addition, a lot of modeling have been proposed to express the observations as described above. However, the problems are still under debate. We have too small amount of materials to discuss about the plant formation, and also have not interpret the whole view of the disk evolution. The most important key is discovering the planet embedded in the disks. It is difficult because the current imaging techniques are able to detect only planets of a few Jupiter mass. Therefore, it is important to interpret the disk property and detail structures, in order to elucidate the uniform view of the disk-planet formation.

Many kinds of complex disk structures that may be excited by embedded planets were introduced in the previous section. They are gap structures, cavities, spirals, and asymmetries (e.g., truncation, surface brightness, pericenter offsets). We need observations to understand the origins of such structures. This study was held in the part of a program that 5 debris disks are observed using Hubble Space Telescope. The purpose of the program is enumerated as follows (see GO 13786 proposal abstract).

1. infer the existence and properties of unseen co-orbiting planets by studying the spatial distribution of dust close to the star

2. constrain dust grain properties and populations as a function of distance from the star

3. constrain the possibilities for planetary system architectures from the dynamical interpretation

4. study small-grain populations from the extended debris features beyond the star

5. obtain highest quality and most complete data for the sake of multi-wavelength investigations in the future

The gaol of this study is to get close to interpret them, especially focusing on the planet effects, by observing a debris disk around HD 141569 A.

15

Chapter 2

Discovery of an Inner Disk Component around HD 141569 A

We report the discovery of a scattering component around the HD 141569 A circumstellar debris system, interior to the previously known inner ring. The discovered inner disk component, obtained in broadband optical light with HST/STIS coronagraphy, was imaged with an inner working angle of $0\rlap{.}''25$, and can be traced from $0\rlap{.}''4$ ($\sim$46 AU) to $1\rlap{.}''0$ ($\sim$116 AU) after deprojection using i=55°. The inner disk component is seen to forward scatter in a manner similar to the previously known rings, has a pericenter offset of $\sim$6 AU, and breaks in its radial surface brightness and infrared surface density distributions. It also has a spiral arm trailing in the same sense as other spiral arms and arcs seen at larger stellocentric distances. The inner disk component spatially overlaps with the previously reported warm CO gas disk seen in thermal emission. We detect no point sources within $2''$($\sim$232 AU), in particular in the gap between the inner disk component and the inner ring. Our upper limit of 9±3 M_J is augmented by a new dynamical limit on single planetary mass bodies in the gap between the inner disk component and the inner ring of 1 M_J, which is broadly consistent with previous estimates.

2.1 Background

This section presents an overview of the HD 141569 system features, based on previous results. HD 141569 A disk has complex structures such as rings/gaps and spirals. One of the origins of exciting such structures is an unseen planet. Therefore, the HD 141569 system is one of the best samples so as to study about the disk-planet interaction. The specification and performance of the data-collection instruments are also discussed.

2.1.1 HD 141569 System

The HD 141569 system is a triplet system located at 116±8 pc from the Sun (van Leeuwen, 2007), and its age is reported to be 5±3 Myr (Weinberger et al., 2000). The spectral type of the primary star, HD 141569 A, is B9.5 (Merín et al., 2004). The two companions (HD 141569 B and C) are M2- and M4-type stars withe projected separations from the primary star of $7\rlap{.}''5$ (∼870 AU) and $8\rlap{.}''9$ (∼1030 AU), respectively (Weinberger et al., 2000). The mid-infrared excess ($\mathrm{L}_{disk}/\mathrm{L}star \sim 8.4\times10^{-1}$) detected by the *Infrared Astronomical Satellite* (IRAS) first suggested that the dust exists around HD 141569 A (Walker & Wolstencroft, 1988; Sylvester et al., 1996). The circumstellar dust disk around HD 141569 A was first resolved by Augereau et al. (1999), who imaged infrared scattered light at 1.6 μm using HST Near Infrared Camera and Multi-Object Spectrometer (NICMOS). At almost the same time, Weinberger et al. (1999) discovered that the disk has two rings, by observing the infrared scattered light (1.1 μm), also using HST/NICMOS. The disk was subsequently imaged in the optical range using the HST Space Telescope Imaging Spectrograph (STIS) and Advanced Camera for Surveys (ACS), by Mouillet et al. (2001) and Clampin et al. (2003), respectively. The disk has also been imaged using ground-based adaptive optics systems (Boccaletti et al., 2003; Janson et al., 2013b; Wahl et al., 2014; Biller et al., 2015; Mazoyer et al., 2016). As a result of these previous studies, the complex structures listed below have been discovered in the HD 141569 A disk. Note again that these studies used optical and near-infrared, and they observed the scattered light from the disk surface.

(i) The disk appears elliptical because this system is inclined towards the line of sight. The inclination and position angle have been reported as i=55° and PA=357°, respectively (Mouillet et al., 2001). Other studies have also reported similar values (Augereau et al., 1999; Weinberger et al., 1999; Clampin et al., 2003).

(ii) An outer ring at $\sim$400 AU with a spiral from north to east has been found.

(iii) An inner ring at $\sim$250 AU with a spiral from north to east, similar to the outer ring and spiral, has been found.

(iv) No dust structures have been detected interior to the inner ring, which is considered to be a cavity inwards $\sim$175 AU.

(v) Two arc-like structures in the north and the south of the outer ring have been observed. These features are considered to be caused by the companions (Clampin et al., 2003).

(vi) The disk has surface brightness asymmetry that is difficult to explain the simple phase function. However, we can see that the east side is brighter than the west side, as a result of a phase difference (e.g., Mouillet et al., 2001). They corrected the surface brightness caused by the phase function, using the brightness ratio of the east to the west. The remained surface brightness asymmetry is due to a difference in surface density (Clampin et al., 2003).

(vii) The disk has a pericenter offset. Clampin et al. (2003) have reported an offset of $<\sim$30 AU between the primary star and the disk center, and Biller et al. (2015) have discovered an offset of $\sim$4 AU between the primary star and the inner ring.

Optical and near-infrared observations have reported the presence of a cavity interior to the inner ring ($<\sim$175 AU). It indicates that there is no sub-micron dust which should be observed as the optical or near-infrared scattered light. However, mid-infrared observations have revealed thermal

emissions from small dust particles within 120 AU of the star (inside the inner ring), in spite of low spatial resolutions. Fisher et al. (2000) have detected extended infrared emission at 10.8 and 18.2 μm using the Observatory Spectrometer and Camera for the Infrared (OSCIR) on Keck II Telescope. Further, Marsh et al. (2002) have mid-infrared imaged the 12.5-, 17.5-, and 20.8-μm circumstellar disk using Mid-InfraRed Large-well Imager (MIRLIN) on Keck II Telescope. In these observations, filters containing polycyclic aromatic hydrocarbon (PAH) were used; therefore, the nature of the material that was detected remains unclear. The mid-infrared emission corresponds to <10 AU; however, the presence of a cavity is unclear due to the low resolution.

This disk is classified as a debris disk based on the infrared excess (Walker & Wolstencroft, 1988; Sylvester et al., 1996); however, there is some remaining gas. Goto et al. (2006) have observed the CO vibration line (ν =2-1 transition) (4.6 μm), and discovered an inner clearing at $\sim$13 AU that is re-calculated by using the recent HD 141569 A distance (van Leeuwen, 2007). According to their results, this warm CO disk ($\sim$10^3 K) is extended at $\sim$59 AU which may be the sensitivity limit of the Infrared Camera and Spectrograph (IRCS) on Subaru Telescope. Further, Thi et al. (2014) detected several kinds of gas emission (OI, CII line) in the mid- and far-infrared using the Photoconductor Array Camera and Spectrometer (PACS) aboard *Hershel* Space Telescope. Péricaud et al. (2014) first resolved CO emissions (^{12}CO (J=2−1) and ^{13}CO (J=2−1)) using the Plateau de Bure Interferometer (PdBI). Flaherty et al. (2016) derived the gas mass between gas-rich primordial disk and gas-poor debris disk by observing ^{12}CO (J=3−2) and ^{12}CO (J=1−0) with SMA and Combined Array for Research in Millimeter-wave Astronomy (CARMA).

Figure 2.1 shows the summary of the previous observation. The HD 141569 system has remained gas, although the disk is classified as a debris disk. The disk also has very complex structures that might be excited by unseen planets. Therefore, the HD 141569 system is very attractive as regards research on star and planet evolution.

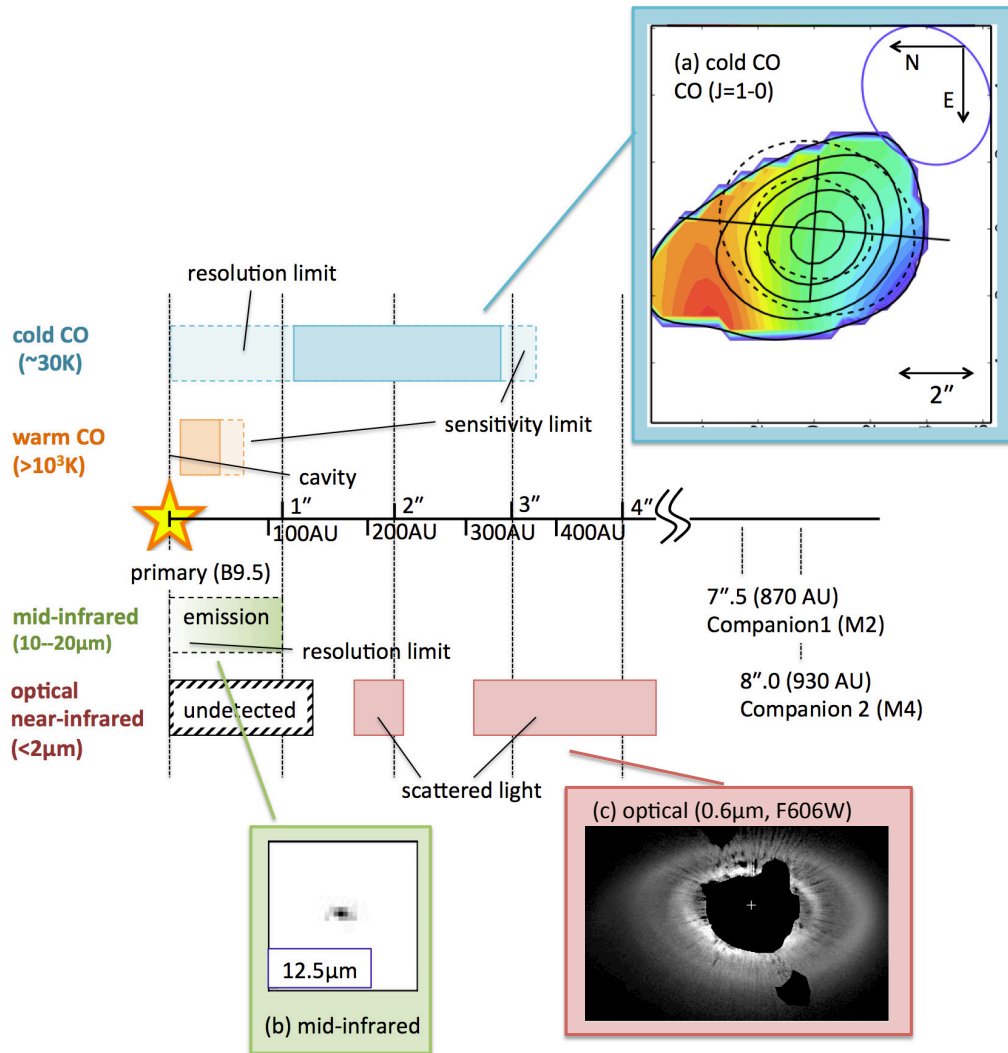Figure 2.1: Architectures of the HD 141569 A disk. Central cartoon is described the gas and dust distribution. (a) cold CO observed by SMA. CO (J=1-0) line (Flaherty et al., 2016). (b) mid-infrared emission (12.5 μm) obtained by Keck Telescope (Marsh et al., 2002). (c) Optical scattered light detected by HST (Clampin et al., 2003). Scales and directions are the same among all image, as described in (a) image.

Table 2.1: STIS CCD performance

Characteristic	Performance
Pixel Format	1024 × 1024 pixels
Field of View	52 × 52 arcseconds
Pixel Plate Scale	0.0507 arcseconds
Wavelength Range	2000–11000Å
Read noise	7.3–7.8 e$^-$ rms at GAIN=4
Saturation Limit	1.44×10^5 e$^-$ at GAIN=4

Note: These values are taken from the STIS Website[1].

2.1.2 Instrument Features: HST/STIS performance

STIS was installed on HST during the second servicing mission (Woodgate et al., 1998). Our observation utilized charge-coupled-device (CCD) detectors without filters referred to as 50CCD apertures. The STIS specifications are listed in Table 2.1, which was obtained from the STIS Website[1].

The 50CCD throughput (CLEAR aperture) is shown in Table 2.2 (see §14.3 in the STIS Instrument Handbook; Biretta, 2015). STIS 50CCD imaging is very sensitive to the spectral type of the observed star, because of its broad bandpass. Figure 2.2 shows the 10000 (∼A0) and 3000 K (∼M5) black-body spectra, which were simulated using the STIS imaging exposure time calculator (ETC)[2]. In this case, the effective wavelengths λ_{eff} differ, at 5530 and 7520 Åfor 10000 and 3000 K, respectively. This has a large influence on the point spread function (PSF)-template subtraction, as will be described in Section 2.2.2.

The thermal problems of HST are generally apparent in the obtained images. The telescope points towards the observation area when the appropriate command is transmitted during observation. This movement causes a slight increase in the telescope/instrument temperature; then, the temperature returns to equilibrium. This effect is known as "breathing", and is apparent in each frame. Generally, the first image of each epoch is noisy and the last is stable. The influence of these effects on our observations will be discussed in Section 2.2.2.

---

[1]http://www.stsci.edu/hst/stis
[2]http://etc.stsci.edu/etc/input/stis/imaging/

Table 2.2: 50CCD Sensitivity and Throughput

Wavelength (Å)	Sensitivity ($\times 10^{15}$)	Throughput (%)
2400	0.141	2.59
3200	0.364	4.99
4000	0.933	10.24
5000	1.60	14.06
6000	1.98	14.50
7000	1.94	12.16
8000	1.46	7.99
9000	1.14	5.55
10200	0.393	1.69

Note: These values are taken from the STIS Website[1].

2.2 Observation

2.2.1 Observation Strategy

Our observation strategy mostly follows that of Schneider et al. (2014), except using much smaller coronagraphic wedge. Two kinds of a coronagraphic wedge are used. One is a large wedge which provides large area deep imaging. In this imagery, the region near the wedge is saturated due to long exposures. Another is a smaller one whose images are generally taken in shorter exposure so as to achieve a smaller inner working angle (IWA). This small-wedge imagery fill in the region saturated in the large-wedge imagery. In addition to this technique, the data are taken at several spacecraft roll angles. There is a region obscured by STIS coronagraphic wedge on these images, which is called the data void. Combining all images after aligned to the celestial north direction makes the data void shrink and reduce decorrelated image artifacts that are stable in the instrument. Thanks to these techniques, we can obtain deep imagery of the whole disk.

2.2.2 PSF-template Subtraction

Obtained images are dominated by the primary star flux. Scattered light by the disk structures is much fainter than the primary star. In order to extract disk structures, the primary star should be removed. We generally employ the
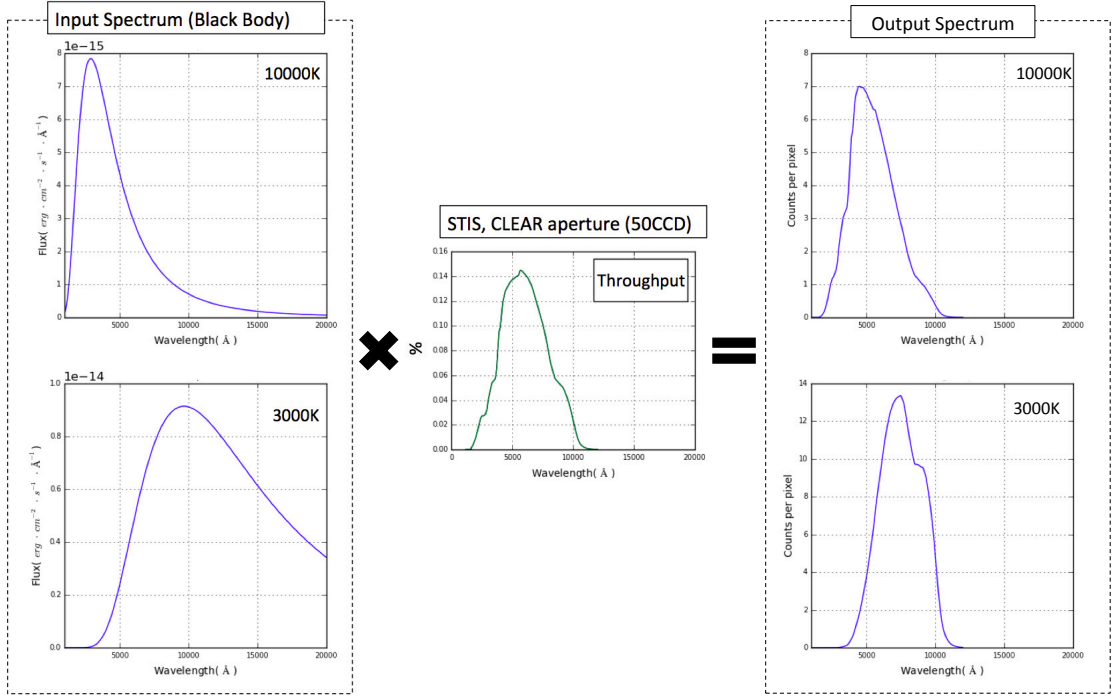
Figure 2.2: STIS ETC simulations. Left panels: black body object spectrum of 10000 K (A0) and 3000 K (M5) which have 15 apparent magnitude in V band. Assumptions of observations are using no filters, 900 s exposure per image, 4 e$^-$ ADU^{-1} gain. Middle panel: throughput of the STIS 50CCD aperture (no filter). Right panels: simulated spectrum taking effects of the throughput in to account.

PSF subtraction method to solve it. A PSF-template star is subtracted from target star images. In case of STIS, the PSF-template star should be selected according to its $B-V$ color because, STIS has a broad bandpass. Moreover, the PSF-template stars should be taken in the same observing epoch of target stars, because of the telescope stability ("breathing" in Section 2.1.2). In the case that observations do not meet these criteria, the primary flux could not be removed sufficiently. Figure 2.3 shows these problems using HD 181327 data which has a narrow debris ring at 88 AU ($\sim$1$''$7) (Schneider et al., 2014). If the data observed in the different epoch used as a PSF-template (Figure 2.3 (b)), then radial streamers, spike-like features from the primary star, are slightly increased compared to the best one (Figure 2.3 (a)). The debris ring are contaminated from heavy radial streamers in Figure 2.3 (c). The PSF-template of this image has a different $B-V$ color, and was obtaied
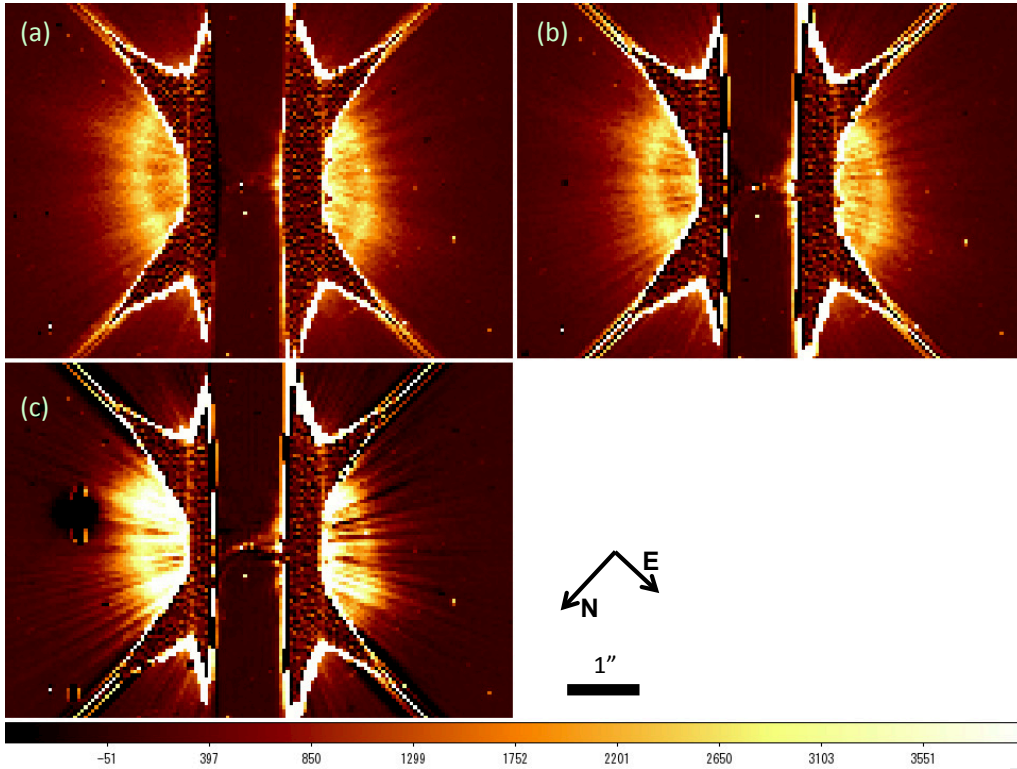
23

Figure 2.3: Examples of PSF subtraction. All are subtracted images of HD 181327 observed on 2011 May 20 (Dataset: obiw11040.fits) using different PSF-templates. (a) using the best PSF-template, HD 180134 ($B-V$=0.45) observed on the same time as the target image (Dataset: obiw13040.fits). (b) using a HD 180134 image observed on 2011 July 10 (Dataset: obiw17040.fits). (c) using the different $B-V$ color and different epoch image, HD 89585 ($B-V$=0.88, 2012 February 19, Dataset: obiw63030.fits).

in the different epoch. In order to detect at smaller IWA, PSF-template stars should be selected carefully.

2.2.3 Our Observation

We observed HD 141569 A and a PSF reference star (HD 135298, A0V[3], $B-V$=0.08) on 2015 Jun 12 and on 2015 August 18, as part of the general observer program (ID: 13786, Principal Investigator: Glenn Schneider). HD 135298 was selected as a PSF reference star because its $B-V$ color

---

[3]Spectral types and magnitudes are taken from SIMBAD (http://simbad.u-strasbg.fr/simbad/).

is similar to HD 141569 A and the celestial distance is not so far ($<15°$). Table 2.3 shows a observation log. We used large and small coronagraphic wedge, WEDGEA1.0 and BAR5 (§12.11 of the STIS instrumental Handbook; Biretta, 2015). WEDGEA1.0 has $1\overset{''}{.}0$ width and provides deep imaging. BAR5 ("the bent finger") was employed as the smaller coronagraphic wedge. This is designed to be achieve $0\overset{''}{.}25$ IWA[4]. Three sets of BAR5 data and one set of WEDGEA1.0 data were taken per visit. For BAR5 observation, three-point dithering (center and ±0.25 pixel perpendicular to the long axis of the bar) were employed to avoid the effects of target mis-centering and to get smallest IWA. The observations were divided into several sub-exposures per set in order to remove cosmic rays ($NUMEXP$ in Table 2.3). We used sub-array readouts to reduce overhead times for many exposures. The field of view (FoV) is 1024 pixels$\times$100 pixels ($52''\times5\overset{''}{.}1$) and 1024 pixels$\times$427 pixels ($52\overset{''}{.}\times22\overset{''}{.}$). The total integration time of HD 141569 A is 9.07×10^2 and 9.67×10^3 seconds in BAR5 and WEDGEA1.0, respectively.

---

[4] "Hubble Space Telescope STIS Coronagraphic BARs",
http://www.stsci.edu/hst/stis/strategies/pushing/coronagraphic_bars

Table 2.3: Observation Log

DATASET[a]	Name	visit#	UT Date	EXPTIME[b]	NUMEXP[c]	TINTTIME[d]	CORONAGRAPH	ORIENTAT[e]	Comments
ocjc31010	HD 141569 A	visit5	2015 August 18	6.3	8	50.4	BAR5	56.53	center dither
ocjc31020	HD 141569 A	visit5	2015 August 18	6.3	8	50.4	BAR5	56.53	plus dither
ocjc31030	HD 141569 A	visit5	2015 August 18	6.3	8	50.4	BAR5	56.53	minus dither
ocjc31040	HD 141569 A	visit5	2015 August 18	405.7	4	1622.8	WEDGEA1.0	56.53	
ocjc32010	HD 141569 A	visit6	2015 August 18	6.3	8	50.4	BAR5	46.53	center dither
ocjc32020	HD 141569 A	visit6	2015 August 18	6.3	8	50.4	BAR5	46.53	plus dither
ocjc32030	HD 141569 A	visit6	2015 August 18	6.3	8	50.4	BAR5	46.53	minus dither
ocjc32040	HD 141569 A	visit6	2015 August 18	405.7	4	1622.8	WEDGEA1.0	46.53	
ocjc33010	HD 135298	visit7	2015 August 18	6.8	8	54.4	BAR5	58.80	center dither
ocjc33020	HD 135298	visit7	2015 August 18	6.8	8	54.4	BAR5	58.80	plus dither
ocjc33030	HD 135298	visit7	2015 August 18	6.8	8	54.4	BAR5	58.80	minus dither
ocjc33040	HD 135298	visit7	2015 August 18	405.5	4	1622	WEDGEA1.0	58.80	
ocjc34010	HD 141569 A	visit8	2015 August 18	6.3	8	50.4	BAR5	36.53	center dither
ocjc34020	HD 141569 A	visit8	2015 August 18	6.3	8	50.4	BAR5	36.53	plus dither
ocjc34030	HD 141569 A	visit8	2015 August 18	6.3	8	50.4	BAR5	36.53	minus dither
ocjc34040	HD 141569 A	visit8	2015 August 18	405.7	4	1622.8	WEDGEA1.0	36.53	minus dither

table continued on the next page.

continued from previous page

DATASET[a]	Name	visit#	UT Date	EXPTIME[b]	NUMEXP[c]	TINTTIME[d]	CORONAGRAPH	ORIENTAT[e]	Comments
ocjc35010	HD 141569 A	visit1	2015 Jun 12	6.3	8	50.4	BAR5	111.53	center dither
ocjc35020	HD 141569 A	visit1	2015 Jun 12	6.3	8	50.4	BAR5	111.53	plus dither
ocjc35030	HD 141569 A	visit1	2015 Jun 12	6.3	8	50.4	BAR5	111.53	minus dither
ocjc35040	HD 141569 A	visit1	2015 Jun 12	400	4	1600	WEDGEA1.0	111.53	
ocjc36010	HD 141569 A	visit2	2015 Jun 12	6.3	8	50.4	BAR5	95.53	center dither
ocjc36020	HD 141569 A	visit2	2015 Jun 12	6.3	8	50.4	BAR5	95.53	plus dither
ocjc36030	HD 141569 A	visit2	2015 Jun 12	6.3	8	50.4	BAR5	95.53	minus dither
ocjc36040	HD 141569 A	visit2	2015 Jun 12	400	4	1600	WEDGEA1.0	95.53	
ocjc37010	HD 135298	visit3	2015 Jun 12	6.8	8	54.4	BAR5	81.01	center dither
ocjc37020	HD 135298	visit3	2015 Jun 12	6.8	8	54.4	BAR5	81.01	plus dither
ocjc37030	HD 135298	visit3	2015 Jun 12	6.8	8	54.4	BAR5	81.01	minus dither
ocjc37040	HD 135298	visit3	2015 Jun 12	400	4	1600	WEDGEA1.0	81.01	
ocjc38010	HD 141569 A	visit4	2015 Jun 12	6.3	8	50.4	BAR5	81.53	center dither
ocjc38020	HD 141569 A	visit4	2015 Jun 12	6.3	8	50.4	BAR5	81.53	plus dither
ocjc38030	HD 141569 A	visit4	2015 Jun 12	6.3	8	50.4	BAR5	81.53	minus dither
ocjc38040	HD 141569 A	visit4	2015 Jun 12	400	4	1600	WEDGEA1.0	81.53	

Note:

a. Same as fits file name and ROOTNAME in the header

b. Individual exposure times (sec).

c. Number of exposures.

d. Total integration time (sec); $EXPTIME \times NUMEXP$

e. Position angle of the image +Y axis measured eastward from celestial north (degree).

2.3 Data Reduction

Our data reduction is held in the order of the exposure-level reduction, PSF-template subtraction and combination of all images. We reduce the same data also by using methods for planet hunting which are powerful to detect point sources.

2.3.1 Exposure-level Reduction

We used the data distributed by HST Archive[5]. For basic instrumental calibration, we made use of the STIS calibration pipeline *calstis* software;s Bostroem & Proffitt, 2011 and calibration reference files provided by Space Telescope Science Institute (STScI). The *calstis* pipeline software performs bias and dark current subtraction, as well as flat-field correction producing "FLT" files in instrumental count units (see Figure 3.5 in STIS Data Handbook Bostroem & Proffitt, 2011).

We combined *NUMEXP* exposures in each set (8 exposures and 4 exposures in WEDGEA1.0) with median. It removes pixels affected by cosmic rays since the positions of affected pixels are different each exposure. In WEDGEA1.0 data, *cosmicrays* task in IRAF (Image Reduction and Analysis Facility) was used to remove the other hot/dead pixels which are not sufficiently got rid of in the procedure of Section 2.3.3. These images shows in Figure 2.4. The instrumental count unit was converted to a count s^{-1} unit by dividing each exposure time (*EXPTIME* in Table 2.3).

2.3.2 PSF-template Subtraction

The stellar PSF was subtracted using the PSF reference star (HD 135298) using the Interactive Data Language (IDL)-based IDP3 (Image Display Paradigm #3; Stobie & Ferro, 2006) software[6]. This step subtracts a scaled and registered PSF reference image from each target (HD 141569 A) images. A difference of B magnitudes was used to scale the brightness. This is because

---

[5]https://archive.stsci.edu/hst/
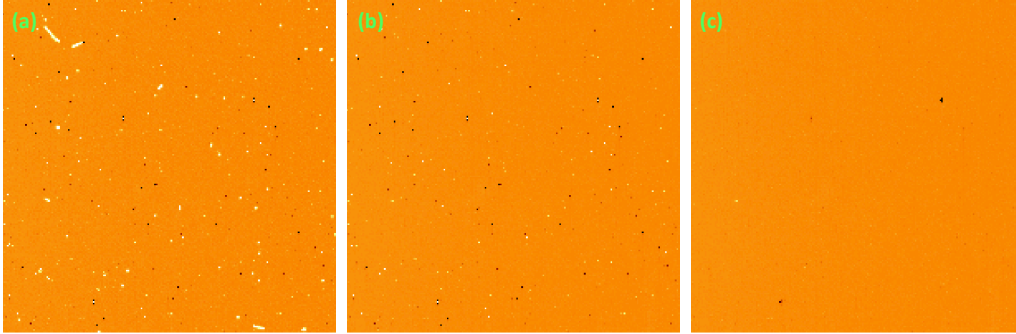[6]https://archive.stsci.edu/prepds/laplace/idp3.html

Figure 2.4: Removing cosmic rays. (a) Zoomed image of WEDGEA1.0 data before median combined (ocjc31040.fits, extension=1). FoV is 200×200 pixels. (b) Median combined image using 4 exposures ($NUMEXP$ in Table 2.3). (c) Median combined image after IRAF/$cosmicrays$ was adapted.

the bandpass is most representative of a B9.5-type star as seen by HST/STIS ($\lambda_{eff} \sim$4400Å), and also because the wavelength does not have the disk flux. The scaling factor was calculated as 1.067 using B=7.20 (HD 141569 A) and B=7.27 (HD 135298) taken from SIMBAD[3]. The position of the star is defined as the crossing point of two diffraction spikes. We extracted coordinates of diffraction spikes in pixel unit, and then fitted them to two line. The crossing points was calculated using the equations of two lines.

The position of the PSF reference star was fine-tuned to minimize the residual of diffraction spikes, after centering by using the center position calculated above. We made subtracted images of all target-PSF template dither combination in BAR5 data. The best one is selected, which is best match the positions between target and PSF-template stars. If not matched, the primary flux near the bar structure is oversubtracted in one side of the bar and undersubtracted in another side. To be more specific, we made 9 subtracted images per visit (3 dithering target images × 3 dithering PSF-template images), and selected one per dithering 3 images. This is shown in Figure 2.5.
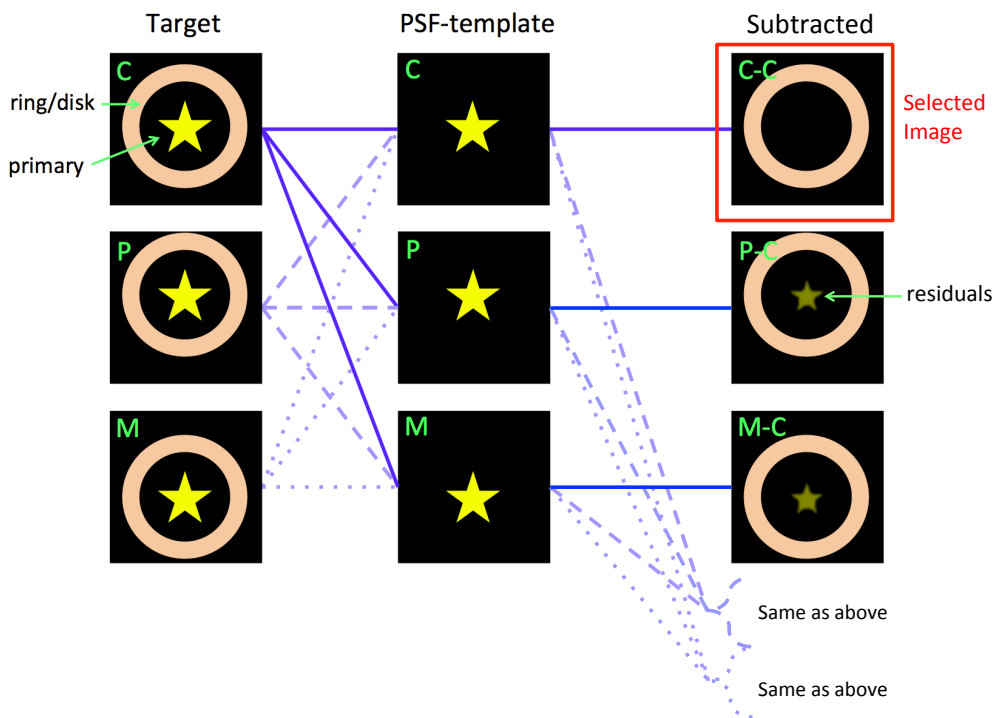
Figure 2.5: Sketch of PSF-subtraction of BAR5, focusing combination written as the blue solid set. "C", "P", and "M" in the figure mean center dithering position, plus dithering position, and minus dithering position, respectively. We selected the best subtracted one in each set.

2.3.3 Combining All Images

After PSF-template subtraction, we made composed imagery. All images were rotated so as to align the celestial north direction. Suitable masks were made for each rotated images using IDP3 Mask Editor to occult non-physical features (diffraction spikes, wedge structures, and saturated pixels) and to mask two companions (HD 141569 B and C). All images were registered to common center, and then median combined so as to remove abnormal (hot or dead) pixels and to shrink the void area. Finally, the BAR5 composite image was inserted in the void area in the WEDGEA1.0 composite image.

2.3.4 Reduction for Extrasolar Planet Hunting

In order to detect point sources with the ground-base telescope mounted an adaptive optics, the angular differential imaging (ADI; Marois et al., 2006) technique is generally used. The imagery is composed of tens/hundreds of short-exposed (~ 10 s^{-1}) images which fix the pupil plane to the detector plane during the observation. This means that each exposure has a different celestial angle in the detector plane, because of the diurnal motion of the observed star. For such imagery, some reduction techniques are proposed, such as classical ADI (Marois et al., 2006), Locally Optimized Combination of Imaging (LOCI, Lafrenière et al., 2007), and Principal Component Analysis (PCA, Amara & Quanz, 2012; Soummer et al., 2012). They are powerful to detect the point sources, but the azimuthally symmetric structures are mostly removed (see Milli et al., 2012). We employed classical ADI and LOCI to search planets in our BAR5 imagery using 6 different roll angles (see Table 2.3), although our data were fewer than those taken in the ground-base observations. The number of BAR5 images is too small to do PCA, so it was not apply to our data set.

A difference between PSF subtraction method and classical ADI/LOCI is how to build a PSF-template image. A PSF-template for classical ADI is the median-combined image of all obtained data set. In LOCI, each obtained image is divided into small sections (generally baumkuchen-like shape), and they are combined by using weighted coefficients which are determined to minimize the residuals between each section and the combined section. The PSF-template for each image are rebuild using combined sections.

We made the PSF template as follow the above procedures by using post-processed and center-aligned data set. The made PSF-template image was subtracted from each target image. After rotated to be common celestial direction between images, PSF-template-subtracted images were combined with median. We note that the same masks as Section 2.3.3 were used in classical ADI, and LOCI does not enployed any masks.

2.3.5 Data Quality

Two M-type Companions

This system has two M-type companions with projected separations of 7″6 and 8″9 from the primary (Weinberger et al., 2000). We estimated the background light contamination due to the two companions. The contamination from the companions' halo is 0.033 count s^{-1}, averaged over the radial profiles of the two companions from 7″ to 8″. The background level is estimated as 0.0032 count s^{-1}, using the median of the pixel values within the area that does not contain the primary, companions, or other background objects. The contamination at the primary position is, at most, 10 times larger than the sky background level. The PSF-template subtraction residuals are 7–50 count s^{-1} at <1″0 from the primary star. This results indicates that the contamination from the companions is significantly smaller than the residuals. Thus, we can conclude that the contamination from the two companions is negligible.

Thermal Condition of Each Visit

Radial streamers are visible in each BAR5 image, particularly for visit1 and visit5. These streamers occurred because the telescope did not reach thermal equilibrium, i.e., they are due to the "breathing" phenomenon (see Section 2.1.2). The last visit of each epoch (visit4 and visit8) is stable. We compared the breathing effect between visit1 (worst) and visit4 (best), using the S/N (signal-to-noise) ratio as the metric. We measured the signal and the noise inside a subsection (radial width: 2 pixel, azimuthal width: 60°), avoiding diffraction spikes. The signal is the median value inside a given section, and the noise is calculated from the standard deviation within that section; hence, the S/N ratios in each subsection can be obtained. The S/N of visit1 and visit4 are ∼1.9 and ∼5.1 (count s^{-1} $pixel^{-1}$) on average for the 0″5–1″0 subsection along the positive y-axis of the detector plane. The best case is ∼2.7 times better than the worst case. Thus, we can evaluate the "breathing" effect.

Position Accuracy

The telescope orientation was altered between two observational epochs was changed. Then, we measured the primary position from the peak position of the diffraction spikes to the fit lines. The difference between both epoch measurements was less than 1 pixel; thus, the telescope was stable for different epochs. From these results, the standard deviation of the fitting is 0.36–0.63 pixels in the x or y direction. Therefore, our measurement accuracy is less than 1 pixel.

2.4 Results

2.4.1 Discovery of an inner disk component

We detect an inner disk component interior to the previously reported rings in all 6 BAR5 observations and the outer extent in WEDGEA1.0 data (Figure 2.6 and Figure 2.7). In PSF-subtracted BAR5 data (Figure 2.6), inner signals are elliptical in shape, aligned with the disk major axis ($PA=357°$ from the north), and move with the sky rotation. This is not the behavior expected from PSF subtraction residuals which are very close to circularly symmetric at low spatial frequencies (Schneider et al., 2014). In other words, elliptical shape is intrinsic to the disk due to the system inclination to the line of sight. In top panels of Figure 2.7, we display the merged BAR5 image, and bottom panels of Figure 2.7 show combined WEDGEA1.0 images of each epoch (Jun and August). We therefore conclude that we have discovered an inner component to HD 141569 A's disk.

The top panel of Figure 2.8 shows the merged WEDGEA1.0 and BAR5 imagery displayed with a stretch optimized for signal within $4''$ of the star. We refer to the outer ring as Component A, the inner ring as Component B, and the newly imaged inner disk component as Component C. We also refer to the gap between Component A and B as Gap AB, and the gap between Component B and C as Gap BC.

Here we summarized Component C briefly. Each is mentioned the following sections in detail. Component C has an outer radial extent of $1''\!.0$, and
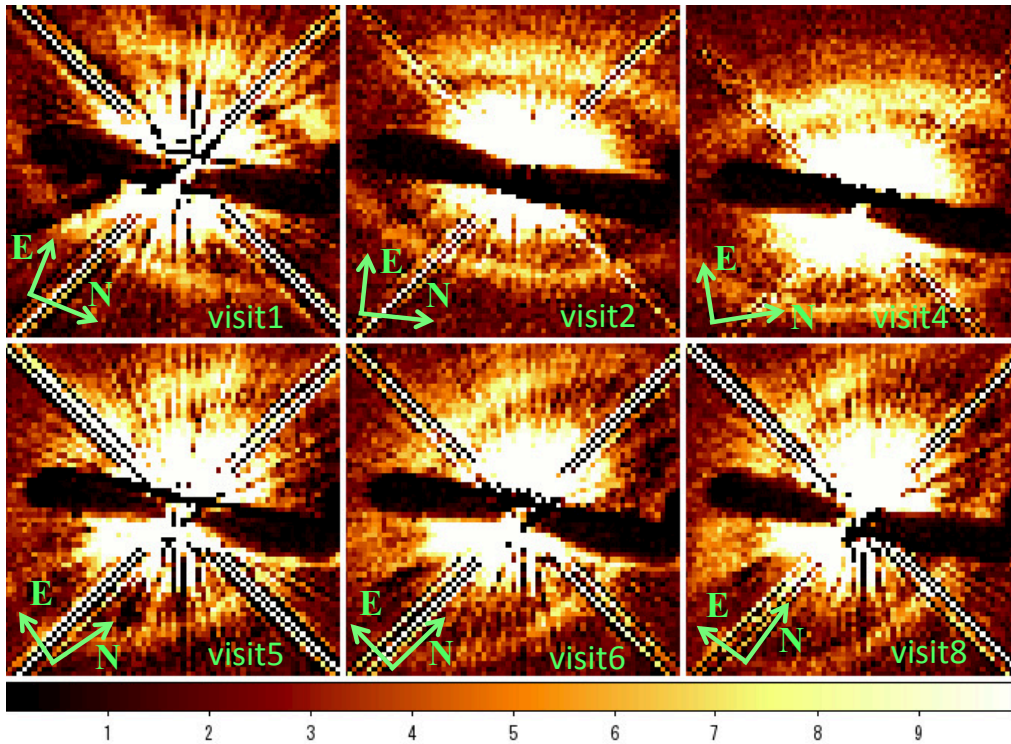
Figure 2.6: PSF-subtracted BAR5 images of all visits. The north direction is different in each image, because of the telescope orientation. FoV is $3\rlap{.}''5 \times 3\rlap{.}''5$. The BAR5 coronagraph structure is a black bar lying in the middle of each panel. A cross mark is made by diffraction spikes. We detected Component C in the all images.

no flux drop down to $0\rlap{.}''25$. This outer edge is defined from breaks seen in the radial surface brightness (SB) profile, which is discussed in Section 2.4.3 in detail. Component C is fully contained interior to Component B. Component C's SB distribution is disk-like, not ring-like as are Component A and B (the width of each components is $\sim 0\rlap{.}''5$ and $\sim 0\rlap{.}''4$ measured along PA=177°). The system inclination is i=55° taken from the previous SITS results (Mouillet et al., 2001). We use this specific angle to deproject the disk. In the surface density (SD) view, Component C has a spiral arm at $1\rlap{.}''1$. This is mentioned in Section 2.4.3.

The top panel of Figure 2.8 shows a final composite image using the method described in Section 2.3, with both the data void and M-type companions masked as black. Figure 2.8 reproduces the previously reported az-
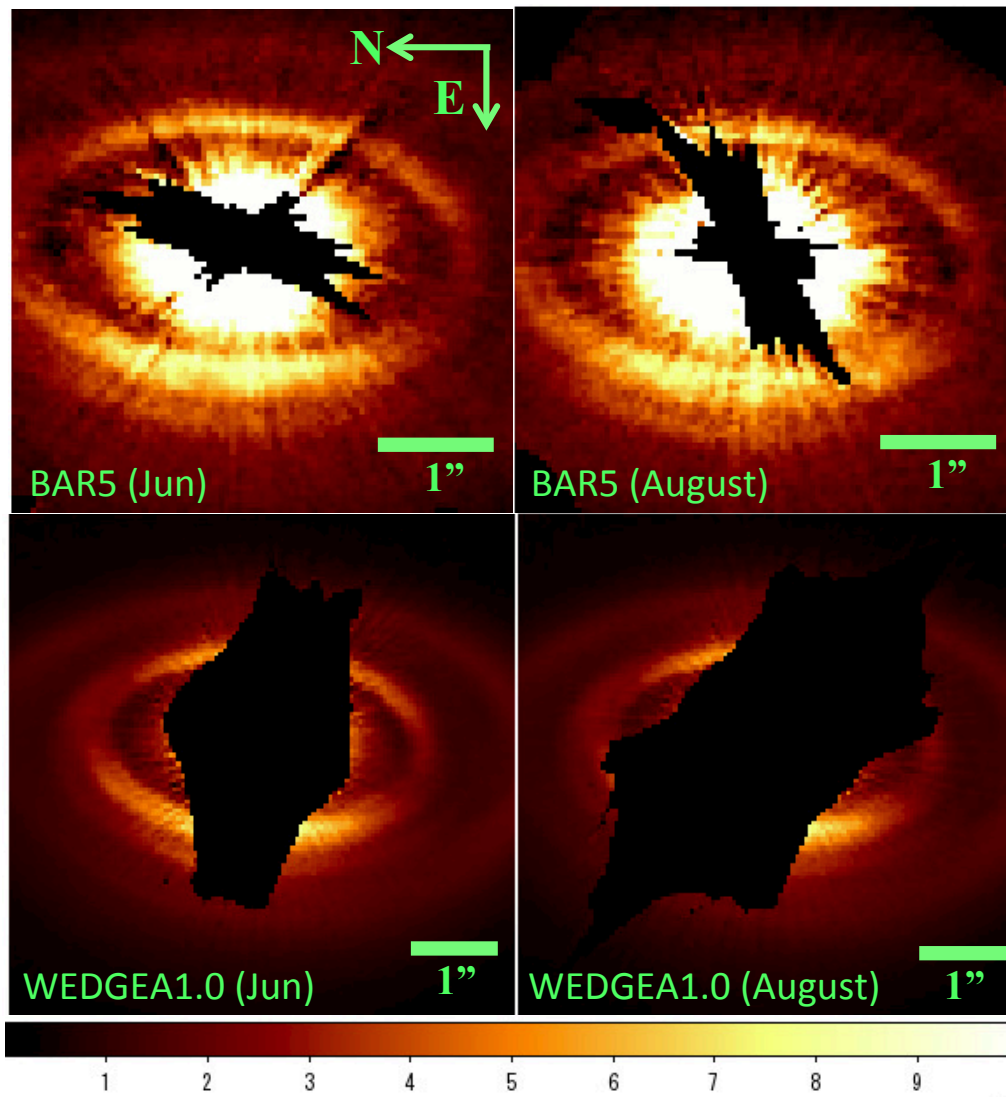
Figure 2.7: Combined images of each coronagraphic wedge and each epoch. Top two panels: combined BAR5 images observed in Jun and August. Bottom two panels: combined WEDGEA1.0 images observed in Jun and August. Data void is shown as black. Note that $1''$ is equal to 116 AU. We detect Component C in the all images.

imuthal brightness asymmetries in Component A and B (Weinberger et al., 1999; Mouillet et al., 2001; Clampin et al., 2003), and suggests that these extend into Component C. For further measurement and analysis for Component C, we deprojected the system using inclination i=55° (see Figure 2.8 (a)), and then follow the Clampin et al. (2003) methodology to correct the phase function and illumination effects. After deprojection of the disk image inclined to our line of sight, the stellocentric mask-limited IWA of our data is 0″.4 (∼46 AU).

2.4.2 Grain forward scattering

We found a similar brightness asymmetry between the east and west for Component C along the disk minor axis as previously reported for Component A and B in the ortical and near-infrared (Weinberger et al., 1999; Mouillet et al., 2001; Clampin et al., 2003). The radial SB of the east side between 0″.7–1″.0 is 2.0±0.1× brighter than that of the west side (SB calculation is described in Section 2.4.3). This is similar to the measured asymmetry in Mouillet et al. (2001) at optical, and slightly larger than Weinberger et al. (1999) at 1.1 μm. We then introduce the Henyey-Greenstein phase function (Henyey & Greenstein, 1941) which is assumed the scattering from a dust. The Henyey-Greenstein phase function is written as,

$$p(\theta, g) = \frac{1}{4\pi} \times \frac{1 - g^2}{[1 + g^2 - 2g\cos\theta]^{3/2}}. \tag{2.1}$$

In this equation, θ is a angle made between the incident light and the scattered light, and g is an anisotropic parameter to be defined by the dust nature, dust size and representative wavelength used in the observation. The g value is from -1 to 1. The forward scattering is stronger than the back scattering if $0 < g \leq 1$, and is weaker if $-1 \leq g < 0$. g=1 is the isotropic scattering. Dust has generally a positive g value[7]. If a geometrically thin disk, the angle (θ) is written as below, using the system inclination (i) and
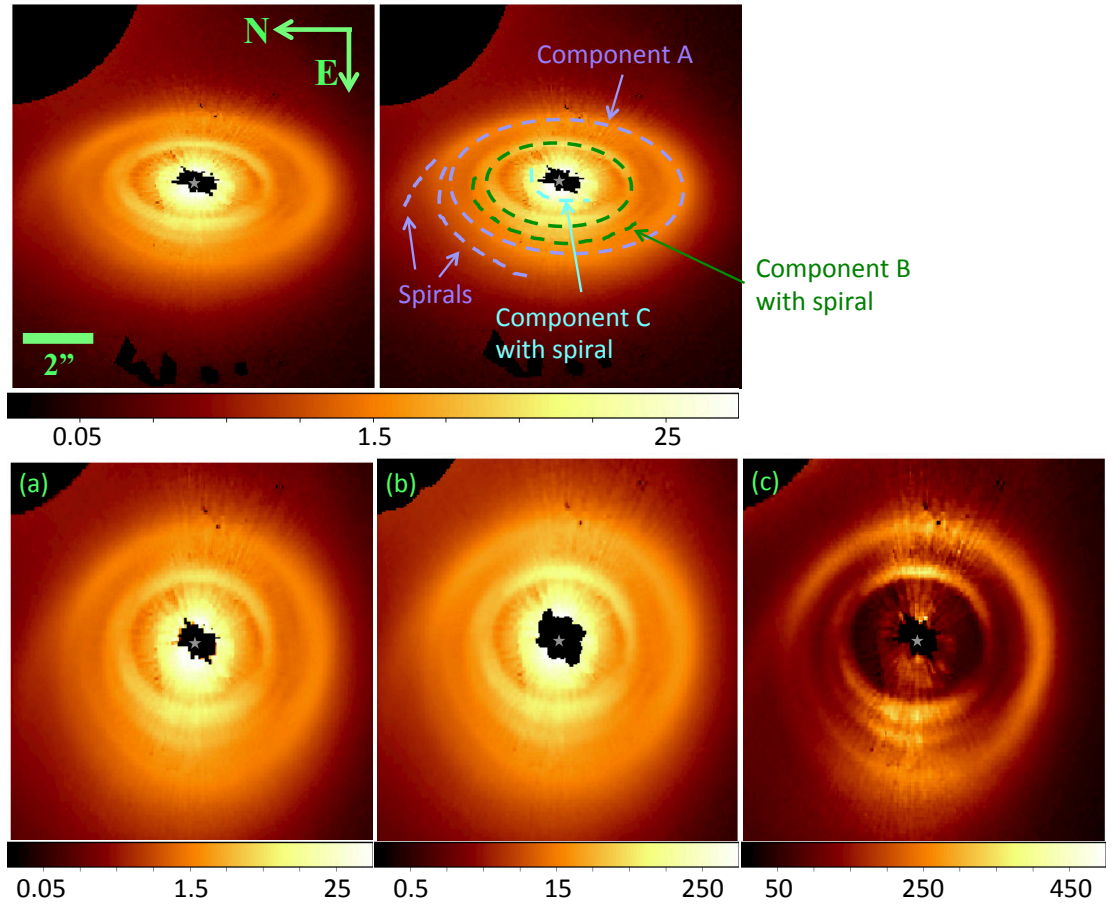
---

[7]see the book, 「大気放射学の基礎」浅野正二著

36

Figure 2.8: Final merged images of HD 141569 A. Top right panel is the same as the top left panel, and shows nomenclatures of each component. (a) Deprojected image of top panel using i=55°. (b) Phase corrected image using g=0.1. (c) Deprojected and phase corrected image multiplied by r^2. Gray stars are the center position of the star. Void area and M-type companions are shown as black (seen in the edge of northwest). The scale unit is count s^{-1}, and the color scale is lognormal except (c) which is linear. Note that 1″ is equal to 116 AU.

a phase angle (ϕ).

$$\cos\theta = \sin i \sin\phi \tag{2.2}$$

The phase angle is measured as counterclockwise, and the near and far side to the Earth are ϕ=90°, and 270°, respectively. The near side is brightest, and the far side is faintest if we assume that the disk is homogeneous and that the star light is anisotropic. However, our results show the strong surface brightness asymmetry that cannot be explained by the simple scattering model. Therefore, we used the typical g value of 0.1 for the correction. The g value is defined by the dust size, composition, and wavelength used in the observation. We used the typical ISM dust size of 0.1 μm and wavelength (2000–10000 Å), then obtained the g value of 0.1, according to the book[7]. Figure 2.8 (b) shows the image after the correction for the scattering phase function asymmetry (g=0.1). This is consistent with the result of Weinberger et al. (1999) and Mouillet et al. (2001). We note that our g value is a lower limit because the degree of forward scattering for debris disks is underestimated (Hedman & Stark, 2015). This problem was addressed in Stark et al. (2014), but it is out of our scope.

We note that our asymmetric ratio of the east to the west corresponds to g=0.14–0.15 assuming i=55° and a geometrically thin disk. Clampin et al. (2003) reported that Component A and B are not azimuthally uniform. Therefore, our strong asymmetry is reasonable features. This is further discussed in Section 2.5.3.

2.4.3 Radial surface density and brightness profile

We multiplied Figure 2.8 (b) by r^2 (arcsec^2) to correct for the radial illumination, which provides a proxy SD map (see Figure 2.8 (c)). In order to investigate detailed structures, the SB and SD profiles were made (Figure 2.9 and Figure 2.10) using the deprojected image and the SD image (Figure 2.8 (a) and (c)). We calculated the mean within each small section (radial: 2 pixels, azimuth: 5°), and converted counts s^{-1} pixel^{-1} to flux density F_λ (erg cm^{-2} s^{-1} Å^{-1} pixel^{-1}) according to the equation described in § 5.3 of Bostroem & Proffitt (2011). Errors on these measurements were calculated

as the 1σ scatter within a section. The SD profile in Figure 2.10 was normalized by the south peak of Component B (2.9×10^{20} erg arcsec^2 cm^{-2} s^{-1} Å^{-1}). We note again that STIS has a broad bandpass and cannot specify a single wavelength. For STIS, 1 count s^{-1} is 4.55×10^{-7} Jy according to Schneider et al. (2014) and one square arcsec is approximately 388 pixels.

The SB of Component C has slope breaks, which are defined as points where the SB drops, along the major axis at $\sim1''$. The location of the breaks is $1''\!.0$ (~116 AU) in the north and $0''\!.9$ (~104 AU) in the south. The difference between the north and south breaks indicates that the Component C center is offset of $0''\!.05$ (~6 AU) toward the north. This is a shift of 1 pixel under the measurement accuracy of sub-pixels. There are no clear breaks in the east and west side in the SB profile of Figure 2.9. It is probably due to an elongation effect introduced by the deprojection. We place no tight constraint on the Component C center along the minor axis, but note that Gap BC is slightly shifted to east according to SB in Figure 2.9. It might be caused by a pericenter offset of Component C, and rigorous investigations are needed to conclude the presence of the pericenter offset.

The SD map (Figure 2.8 (c)) and the SD profile (Figure 2.10) shows the presence of a spiral arm. It locates at $1''\!.1$ (~128 AU) and seen from the north to the east. The feature is the same sense as the outer spirals of Component A and Component B, which is the matrioshka-like structure.

2.4.4 Sensitivity to exoplanets

Our results of detected Component C reveal the clear gap (Gap BC) between Component B and Component C. Gaps are considered to be opened by forming giant planets. We detected no point sources within $2''$ (~232 AU) of the star in the PSF-template subtracted image, especially in Gap BC. We calculated the sensitivity to exoplanets that may exist within the disk and report our sensitivity limits (See Brandt et al., 2013 in detail).

The sensitivity limits are the 5σ noise which was produced by multiplying standard deviations by 5. The standard deviations are typically measured within pixels in each ring, assuming the point symmetry with respect to the
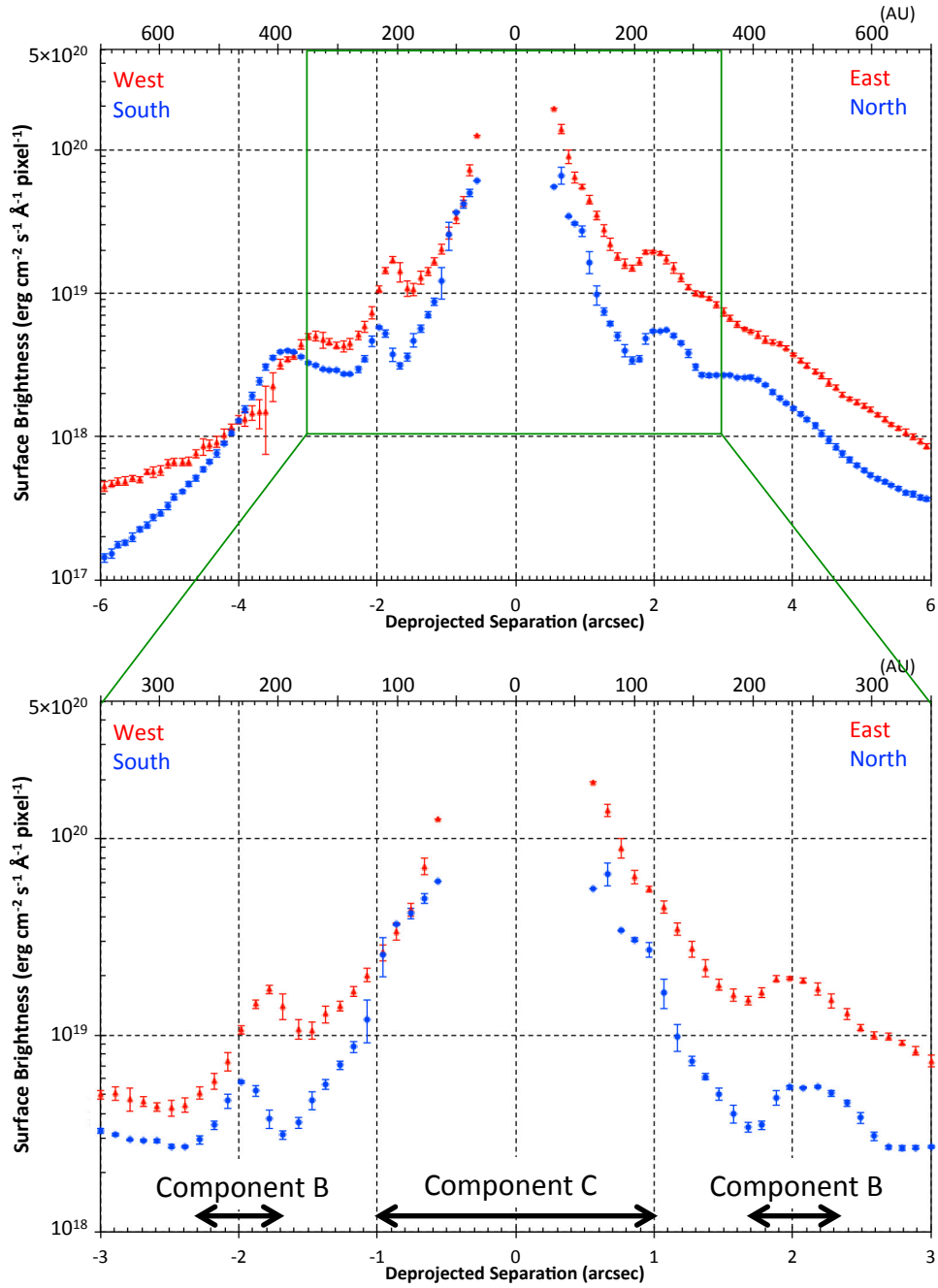
Figure 2.9: Surface Brightness profile along with the major and minor axis. There are breaks at 1″0, no flux drop at inner most region, and a pericenter offset towards the north.
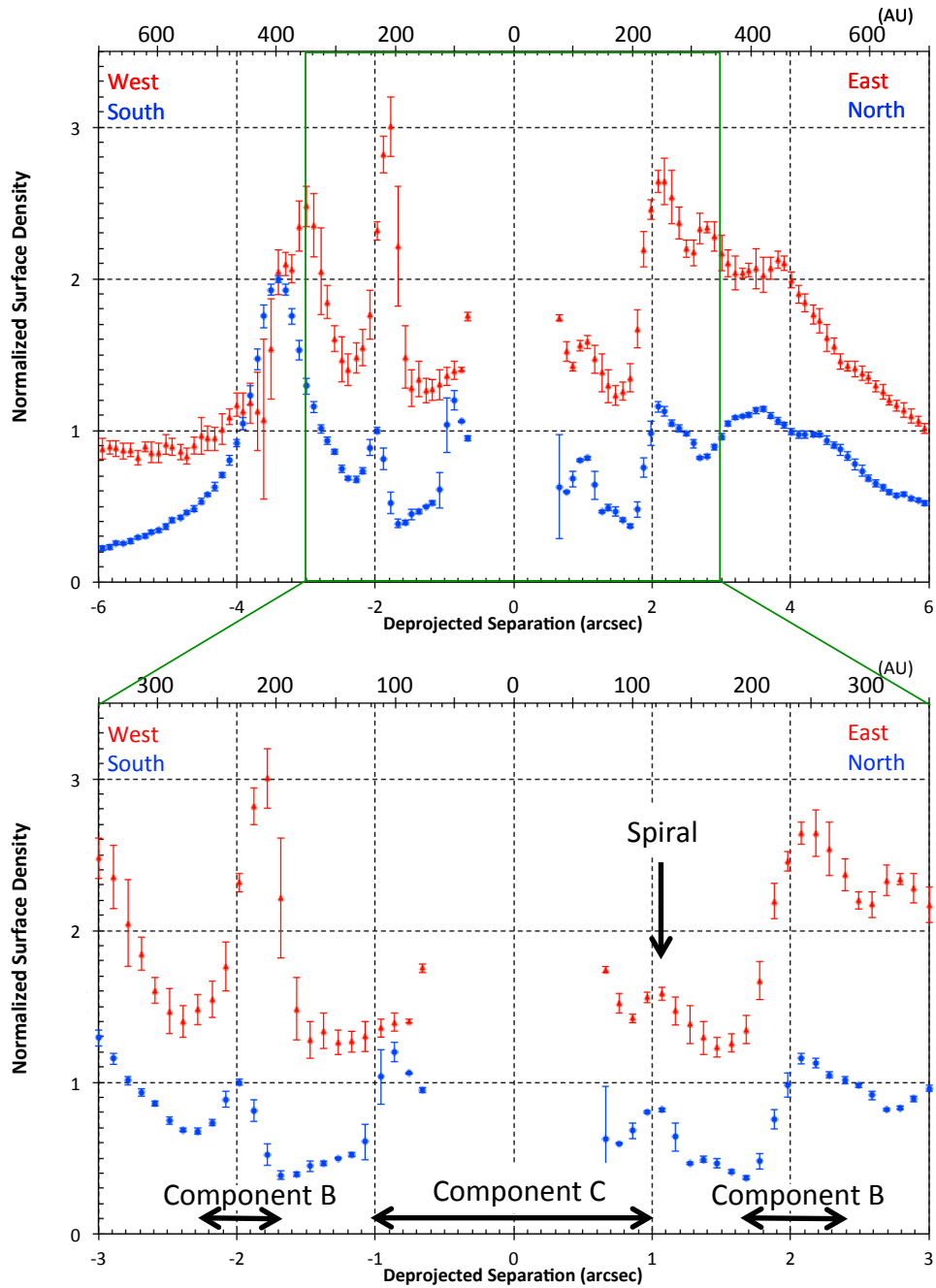
Figure 2.10: Normalized surface density profile along with the major and minor axis. South ring at 2″ is used for the normalization. There is a spiral at 1″.1.
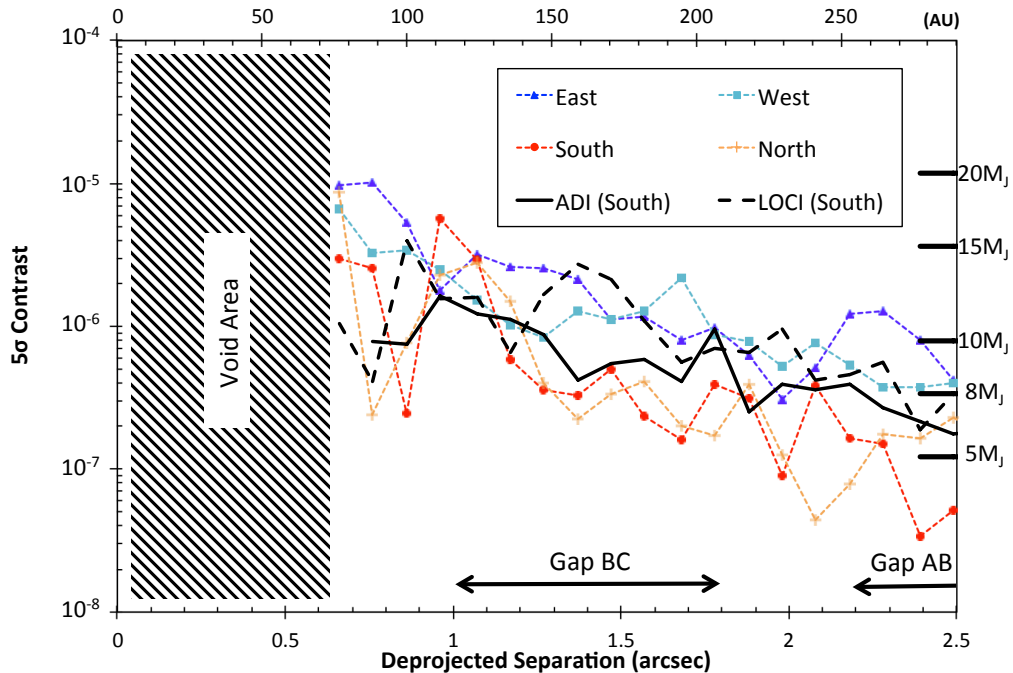
Figure 2.11: Detection limits on exoplanets. The vertical axis is the 5σ contrast relative to the primary star. The horizontal axis is deprojected separation from the primary star. The right axis shows the corresponding mass estimates used BT Settl modeling. Calculation method is described in Section 2.4.4.

primary star. Our data has complex disk structures, and thus we calculated the sensitivity limits in each direction using small sections employed in Section 2.4.3, not rings. The 1σ noise was calculated from the standard deviation within each small section (radial: 2 pixels, azimuth: 5°, same ones as Section 2.4.3). This is assumed that point sources are detected only the core of the PSF (1 pixel). Figure 2.11 shows the 5σ ($5\times1\sigma$) contrast curve, which we consider the sensitivity limit of the observations. To make a contrast relative to the primary, the primary star count rate for our observation was estimated using the STIS imaging ETC[2] since the primary star was occulted by wedge structures. We used a template A0-type spectrum with extinction $B - V$=0.1, and normalized it using the V magnitude of HD 141569 A. Then the 5σ noise was divided by the estimated primary star's count rate (2.1×10^6 count s^{-1}).

Exoplanetary mass estimates are shown in the right side of Figure 2.11.

42

They were estimated from the BT Settl evolutionary model (e.g., Allard et al., 2011). We first consulted surface gravities and effective temperatures of sub-stellar objects (5, 8, 10, 15, and 20 M_J) at 5 Myr, according to the BT Settl model. The spectra of the objects were taken from the Phoenix web simulator[8]. Using the spectra and STIS imaging ETC[2], we estimated the count values in STIS if we observed them with the same observational conditions (e.g., exposure time, distance of the target star, and inter stellar extinction). Each contrast converted by the primary brightness is shown in Figure 2.11.

With our results, the PSF core of the possible planet is 4.4–0.5 counts s^{-1} in Gap BC. It corresponds to the contrast of point sources from 2.1×10^{-6} down to 2.4×10^{-7}. Converted to mass, we conclude that our luminosity upper limit corresponds to a mass upper limit of 9 ± 3 M_J. We also embedded some artificial planets and confirmed that our detection limit was reasonable.

There are no point sources although using the classical ADI and LOCI (see Figure 2.12). Their sensitivity limits (only south direction) are also shown in Figure 2.11, employed the same calculation as described above. They did not show a great improvement of sensitivity limits. This is because the small number of images used in these analysis techniques.

2.5 Discussion

2.5.1 Why can we detect the inner disk component?

We detected an inner disk component (Component C) in broadband, optical scattered light. It has similar scattering properties to outer components (A and B), and is imaged at stellocentric distances from $0\overset{''}{.}4$ ($\sim$46 AU) to $1\overset{''}{.}0$ ($\sim$116 AU) with a spiral arm ($1\overset{''}{.}1$, $\sim$128 AU) after deprojection. The previous studies, however, could not detected Component C. Compared with the previous STIS imagery, Mouillet et al. (2001) did not recover Component C due to the wedge occultation. Component C is also fully masked in the ACS observations reported by Clampin et al. (2003).
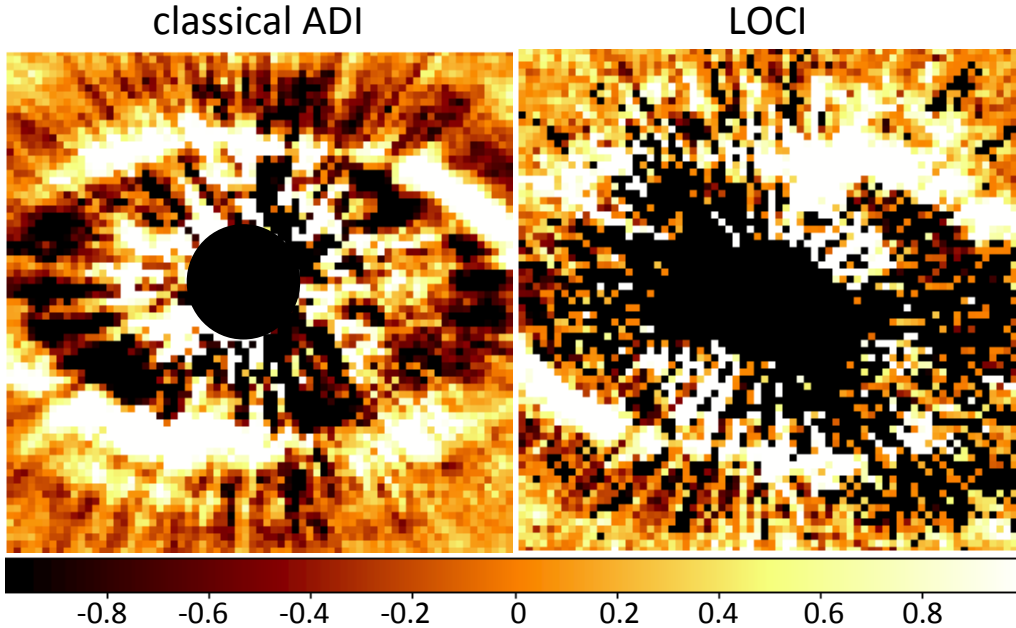
---

[8]https://phoenix.ens-lyon.fr/simulator/index.faces

Figure 2.12: Final image used ADI analysis techniques. Left: classical ADI. Right: LOCI. FoV is $3''\!.5 \times 3''\!.5$. North is left and East is down. Color scale is linear. Data void is shown as black.

The IWA of ground-base observations has reached $0''\!.3$ at best (Boccaletti et al., 2003; Janson et al., 2013b; Wahl et al., 2014; Biller et al., 2015), but they did not report the presence of Component C. They used ADI observations and analysis methods, which are considered to derive a self subtraction of Component C. Figure 2.12 cannot recover the flux of Component C, and also caused distortions of Component B. We measured a ratio of calssical ADI or LOCI to PSF-template subtraction method. We conclude that the sensitivity to faint structures at the small IWA are more difficult to recover with the ADI processing; therefore the previous ground-base observation could not detect Component C. We note that VLT Nasmyth Adaptive Optics System Near-Infrared Imager and Spectrograph (NaCo) and GPI succeed to detect Component C structure, and they are now under discussion (Currie et al, in prep; GPI members, in prep.).

2.5.2 Gas disk and small grain disk

Our imaged Component C overlaps partially with the disk seen in mid-infrared thermal emission at 10.8 μm (Fisher et al., 2000) and 12.5 μm (Marsh et al., 2002). A warm disk in CO emission was detected by Goto et al. (2006) at 13–59 AU based on more recent stellar parallax from van Leeuwen (2007). Their outer radius reflects a sensitivity limit. The Component C material we now see in scattered light is, in part, in the same stellocentric region as the CO emission. A spatial overlap of especially small-grain dust and gas is expected in a transitional disk. Our results might indicate that the HD 141569 system is on the stage evolving from a transitional disk to a debris disk, because the system has both disk characteristics.

Péricaud et al. (2014) fit the SED of HD 141569 A using three single-temperature dust black bodies at 1000, 350, and 100 K. These components correspond to dust within ∼15 AU of the star using the equilibrium temperature from blackbody grains. These distances can be up to a factor of 4 larger for low dust masses if the grains are small and heating of PAHs by transient absorption of ultraviolet photons is neglected (Moór et al., 2015). In this scenario, the dust may reside at distances as far as ∼60 AU. Although this estimates are the simple calculation, these results suggest that significant dust may exist interior to our imaged Component C. There are other studies in which detail fittings were done (e.g., Li & Lunine, 2003; Merín et al., 2004). For example, Merín et al. (2004) used more realistic model to fit the disk from 0.24 to 428 AU, and obtained the solution that could described the whole range of its SED. These results are also consistent with the presence of Component C.

2.5.3 Brightness asymmetry

As mentioned in Section 2.4.2, there is an azimuth asymmetry in the radial SB. This feature is discussed further in this subsection, although g=0.1 is a reasonable and conservative value for the general dust grains. If the simple model disk is assumed (homogeneous disk and anisotropic star irradiation), the near and far sides relative to the Earth are brighter and fainter, respec-

tively, among the regions that are the same distance from the primary star. However, our observations indicate that the north and south regions (along the major axis) are faint compared to the east and west regions (along the minor axis). Thus, a contradiction is obtained even if a geometrically thin disk is employed. The flared profile is another typical disk shape. In the case of a flared disk, the angle θ is expressed as below, using the scale height ($h(r)$) at the distance from the primary star (r). However, even if this equation is assumed, the brightness asymmetry cannot be represented.

$$\cos\theta = \frac{r\sin\phi\sin i + h(r)\cos i}{\sqrt{r^2 + h(r)^2}}. \tag{2.3}$$

Two facts are considered to cause brightness asymmetry: a difference in the surface density at each position, and a difference in the amount of light reaching each position. Certain structures on the disk (e.g., walls and wraps) generally observed in protoplanetaly disks have been reported to cause such variability (e.g., Bouvier et al., 2007). In addition, inclination of the inner disk against the outer rings might be another cause of this asymmetry. These structures may also cause asymmetric illumination on disks. Their effects are degenerate, and cause of the brightness asymmetry cannot be determined conclusively at this stage. However, discovered Component C would support that irradiation from the star is not isotropic.

2.5.4 Dynamical Limit on Planet Mass

Planets can open gaps in particle disks via resonance overlap. Ardila et al. (2005) used numerical models of the gas and dust to demonstrate that a very eccentric ($e = 0.6$), 5 M_J planet could clear the observed inner cavity (inside Component B) in the disk. Reche et al. (2009) investigated the effects of two giant planets orbiting in the disk using N-body simulations and found that a 2 M_J planet with $e = 0.2$ could clear the inner cavity while a low-eccentricity ($e = 0.05$), 0.2 M_J mass planet orbiting for 5 Myr could clear the outer gap. Wisdom (1980) used the resonance overlap criterion to analytically derive the relationship between the width of a gap and the mass of the planet in a

collisionless disk. Nesvold & Kuchner (2015) used numerical simulations of a collisional disk to estimate a time-dependent gap law. This collisional gap law is based on gas-free N-body simulations of a planetesimal belt and does not consider the effects of gas drag or radiation pressure on dust dynamics, all of which may be important in the case of HD 141569. However, Ardila et al. (2005) simulated the effects of both gas drag and radiative forces on the dust in HD 141569 A. Therein they found that their simulated planetesimal distribution resembled the observed dust distribution. The gap law can be used to place upper limits on the mass of a planet orbiting in a gap, but it is limited by a degeneracy between the planet mass and the radial distance between the planet and the gap. Because we measure the location of both the inner and outer edge of the gap in the HD 141569 A disk, we can break this degeneracy by assuming that the gap contains a planet on a circular orbit at the midpoint between the gap edges (137.5 AU for Gap BC). Assuming a system age of 5 Myr and stellar mass of 2.5 $M_\odot$ (Weinberger et al., 2000), and estimating the vertical optical depth of the disk as $L_{IR}/L_{star} = 1.8 \times 10^{-2}$ (Merín et al., 2004), we use the technique of Nesvold & Kuchner (2015) to place an upper limit of 1 M_J on a hypothetical planet orbiting in Gap BC. The model proposed by Nesvold & Kuchner (2015) does not include gas. HD 141569 has remained gas, but the gas is low ($M_{gas} < 10^{-4}$ $M_\odot$). Therefore, the employment of this model is reasonable to HD 141569 A debris disk.

Because we detect a hot dust population close to the star, we are able to constrain the size of Gap BC and therefore our upper limit for the planet in Gap BC, 1 M_J, is smaller than those of Ardila et al. (2005) and Reche et al. (2009). Our estimate for the mass of the outer planet is remarkably similar to that of Reche et al. (2009); however, they found that planet masses of 2 M_J for the inner planets, and 0.2 M_J for the inner and outer planets, respectively resulted in too low a mass for the belt between the two planets. Further numerical simulations are needed to determine the best-fit system architecture to explain the dust distribution in the disk.

We also used the method described in Rodigas et al. (2014) which is more easiest estimation, for confirmation. The upper limit of 5.7 M_J is estimated in Gap BC using the normalized FWHM (Full Width at Half Maximum) of

Component B (0.″15). This is a bit massive than that estimated by Nesvold & Kuchner (2015), but they are generally consistent.

2.6   Summary

We observed the HD 141569 A debris disk using HST/STIS, and discovered the inner disk component (Component C) inside the previously known structures (rings and spirals). The characteristics of Component C as listed below.

1. Component C extends from 0.″25 to 1.″0.

2. Component C exhibits the similar scattering features to the outer rings (Components A and B). The surface brightness is asymmetric.

3. Break points exist, at which the slope of the surface brightness changes.

4. The disk center and the primary position may differ, which means a pericenter offset towards the north.

5. A spiral structure (1.″1, $\sim$128 AU) similar to the outer spiral in apperent.

6. Our detected Component C overlaps the previously observed CO disk.

In addition, we detected no point sources massive than 9$\pm$3 M$_J$ in Gap BC (between Components B and C). The dynamical model limits the planet detection as <1 M$_J$.

Chapter 3

Summary

The debris disk around HD 141569 A has complex structures such as rings/gap, spirals, and pericenter offsets and also the gas is still remained. There are some intricate disks observed to date, and HD 141569 A is one of them. This picture cannot be explained by the simple model. In addition, only our study cannot reveals the disk-planet interaction. Both precious observations of gas and dust and modelings are very important in order to interpret the whole view of the disk evolution.

Our results first reveal the presence of a gap between Component B and Component C (Gap BC). The gap might be produced not only by the forming planet but also by the gravitational instability. However, there is a high possibility that the origin of the spiral and a pericenter offset is the unseen planet. We detected no point sources massive than 9 ± 3 M$_J$ in Gap BC. The dynamical model limits the planet mass of <1 M$_J$ which may open the gap. The model limit is lower than our detection limit. Therefore, our observation cannot detect embedded planet in Gap BC. We note that there is a possibility that the detected spiral is a sign of the circumplanetary disk material, but we cannot confirm the scenario at the present stage.

Complex structures and asymmetric features detected in the HD 141569 A disk is strongly support the presence of planets. It is, however, hard to conclude it only the current information. Our observation did not reach the smaller IWA and the better detection limit on planets, to discover the inner

cavity of Component C and planets. The next generation instruments will be necessary in order to detect such planets. The extreme adaptive optics (AO) systems will be worked for this purpose, such as GPI, SPHERE, and SCExAO (the Subaru Coronagraphic Extreme AO). Especially for GPI, polarization can be obtained. It works well to detect and to discuss Component C nature in detail. On the other hand from the space, the next generation telescope, James Webb Space Telescope (JWST), will be launched within a few years. They are powerful to discuss more detail structures of disks and planets relationships.

Acknowledgements

References

Alexander, R. D., Clarke, C. J., & Pringle, J. E. 2006, MNRAS, 369, 229

Allard, F., Homeier, D., & Freytag, B. 2011, in Astronomical Society of the Pacific Conference Series, Vol. 448, 16th Cambridge Workshop on Cool Stars, Stellar Systems, and the Sun, ed. C. Johns-Krull, M. K. Browning, & A. A. West, 91

ALMA Partnership, Brogan, C. L., Pérez, L. M., et al. 2015, ApJ, 808, L3

Amara, A., & Quanz, S. P. 2012, MNRAS, 427, 948

Andrews, S. M. 2015, PASP, 127, 961

Ardila, D. R., Lubow, S. H., Golimowski, D. A., et al. 2005, ApJ, 627, 986

Artymowicz, P., & Lubow, S. H. 1994, ApJ, 421, 651

Augereau, J. C., Lagrange, A. M., Mouillet, D., & Ménard, F. 1999, A&A, 350, L51

Bachiller, R. 1996, ARA&A, 34, 111

Benisty, M., Juhasz, A., Boccaletti, A., et al. 2015, A&A, 578, L6

Biller, B. A., Liu, M. C., Rice, K., et al. 2015, MNRAS, 450, 4446

Biretta, J. 2015, STIS Instrument Handbook, Version 14.0

Blandford, R. D., & Payne, D. G. 1982, MNRAS, 199, 883

Boccaletti, A., Augereau, J.-C., Marchis, F., & Hahn, J. 2003, ApJ, 585, 494

Bonnefoy, M., Zurlo, A., Baudino, J. L., et al. 2015, ArXiv e-prints, 1511.04082

Bostroem, K. A., & Proffitt, C. 2011, STIS Data Handbook v. 6.0

Bouvier, J., Alencar, S. H. P., Boutelier, T., et al. 2007, A&A, 463, 1017

Brandt, T. D., McElwain, M. W., Turner, E. L., et al. 2013, ApJ, 764, 183

Brown, J. M., Blake, G. A., Dullemond, C. P., et al. 2007, ApJ, 664, L107

Brown, J. M., Blake, G. A., Qi, C., et al. 2009, ApJ, 704, 496

Burrows, C. J., Stapelfeldt, K. R., Watson, A. M., et al. 1996, ApJ, 473, 437

Clampin, M., Krist, J. E., Ardila, D. R., et al. 2003, AJ, 126, 385

Clarke, C. J., Gendrin, A., & Sotomayor, M. 2001, MNRAS, 328, 485

Dent, W. R. F., Wyatt, M. C., Roberge, A., et al. 2014, Science, 343, 1490

Dong, R., Zhu, Z., Fung, J., et al. 2016, ApJ, 816, L12

Dong, R., Zhu, Z., Rafikov, R. R., & Stone, J. M. 2015, ApJ, 809, L5

Dullemond, C. P., & Dominik, C. 2005, A&A, 434, 971

Fisher, R. S., Telesco, C. M., Piña, R. K., Knacke, R. F., & Wyatt, M. C. 2000, ApJ, 532, L141

Flaherty, K. M., Hughes, A. M., Andrews, S. M., et al. 2016, ArXiv e-prints, 1601.02642

Fukagawa, M., Hayashi, M., Tamura, M., et al. 2004, ApJ, 605, L53

Golimowski, D. A., Ardila, D. R., Krist, J. E., et al. 2006, AJ, 131, 3109

Goto, M., Usuda, T., Dullemond, C. P., et al. 2006, ApJ, 652, 758

Hayashi, C., Nakazawa, K., & Nakagawa, Y. 1985, in Protostars and Planets II, ed. D. C. Black & M. S. Matthews, 1100

Hedman, M. M., & Stark, C. C. 2015, ApJ, 811, 67

Henyey, L. G., & Greenstein, J. L. 1941, ApJ, 93, 70

Ingraham, P., Marley, M. S., Saumon, D., et al. 2014, ApJ, 794, L15

Ireland, M. J., & Kraus, A. L. 2008, ApJ, 678, L59

Janson, M., Brandt, T. D., Kuzuhara, M., et al. 2013a, ApJ, 778, L4

Janson, M., Brandt, T. D., Moro-Martín, A., et al. 2013b, ApJ, 773, 73

Kanagawa, K. D., Muto, T., Tanaka, H., et al. 2015a, ApJ, 806, L15

Kanagawa, K. D., Tanaka, H., Muto, T., Tanigawa, T., & Takeuchi, T. 2015b, MNRAS, 448, 994

Knapp, G. R., & Kerr, F. J. 1974, A&A, 35, 361

Kuzuhara, M., Tamura, M., Kudo, T., et al. 2013, ApJ, 774, 11

Lafrenière, D., Marois, C., Doyon, R., Nadeau, D., & Artigau, É. 2007, ApJ, 660, 770

Li, A., & Lunine, J. I. 2003, ApJ, 594, 987

Liffman, K. 2003, Publications of the Astronomical Society of Australia, 20, 337

Lubow, S. H., & D'Angelo, G. 2006, ApJ, 641, 526

Macintosh, B., Graham, J. R., Ingraham, P., et al. 2014, Proceedings of the National Academy of Science, 111, 12661

Marois, C., Lafrenière, D., Doyon, R., Macintosh, B., & Nadeau, D. 2006, ApJ, 641, 556

Marois, C., Macintosh, B., Barman, T., et al. 2008, Science, 322, 1348

Marois, C., Zuckerman, B., Konopacky, Q. M., Macintosh, B., & Barman, T. 2010, Nature, 468, 1080

Marsh, K. A., Silverstone, M. D., Becklin, E. E., et al. 2002, ApJ, 573, 425

Mayama, S., Hashimoto, J., Muto, T., et al. 2012, ApJ, 760, L26

Mayor, M., & Queloz, D. 1995, Nature, 378, 355

Mazoyer, J., Boccaletti, A., Choquet, E., et al. 2016, ArXiv e-prints, 1601.00505

Merín, B., Montesinos, B., Eiroa, C., et al. 2004, A&A, 419, 301

Milli, J., Mouillet, D., Lagrange, A.-M., et al. 2012, A&A, 545, A111

Momose, M., Morita, A., Fukagawa, M., et al. 2015, PASJ, 67, 83

Moór, A., Henning, T., Juhász, A., et al. 2015, ApJ, 814, 42

Moór, A., Juhász, A., Kóspál, Á., et al. 2013, ApJ, 777, L25

Mouillet, D., Lagrange, A. M., Augereau, J. C., & Ménard, F. 2001, A&A, 372, L61

Muto, T., Grady, C. A., Hashimoto, J., et al. 2012, ApJ, 748, L22

Nelson, A. F., Benz, W., Adams, F. C., & Arnett, D. 1998, ApJ, 502, 342

Nesvold, E. R., & Kuchner, M. J. 2015, ApJ, 798, 83

Nettelmann, N., Fortney, J. J., Kramm, U., & Redmer, R. 2011, ApJ, 733, 2

Oppenheimer, B. R., Baranec, C., Beichman, C., et al. 2013, ApJ, 768, 24

Péricaud, J., Di Folco, E., Dutrey, A., et al. 2014, in Thirty years of Beta Pic and Debris Disks Studies, 58

Perrin, M. D., Duchene, G., Millar-Blanchaer, M., et al. 2015, ApJ, 799, 182

Piétu, V., Guilloteau, S., & Dutrey, A. 2005, A&A, 443, 945

Qi, C., Ho, P. T. P., Wilner, D. J., et al. 2004, ApJ, 616, L11

Reche, R., Beust, H., & Augereau, J.-C. 2009, A&A, 493, 661

Rodigas, T. J., Malhotra, R., & Hinz, P. M. 2014, ApJ, 780, 65

Schneider, G., Grady, C. A., Hines, D. C., et al. 2014, AJ, 148, 59

Schneider, G., Smith, B. A., Becklin, E. E., et al. 1999, ApJ, 513, L127

Schneider, G., Weinberger, A. J., Becklin, E. E., Debes, J. H., & Smith, B. A. 2009, AJ, 137, 53

Shakura, N. I., & Sunyaev, R. A. 1973, A&A, 24, 337

Skemer, A. J., Morley, C. V., Zimmerman, N. T., et al. 2015, ArXiv e-prints, 1511.09183

Snellen, I. A. G., Brandl, B. R., de Kok, R. J., et al. 2014, Nature, 509, 63

Soummer, R., Pueyo, L., & Larkin, J. 2012, ApJ, 755, L28

Stark, C. C., Schneider, G., Weinberger, A. J., et al. 2014, ApJ, 789, 58

Stobie, E., & Ferro, A. 2006, in Astronomical Society of the Pacific Conference Series, Vol. 351, Astronomical Data Analysis Software and Systems XV, ed. C. Gabriel, C. Arviset, D. Ponz, & S. Enrique, 540

Strom, K. M., Strom, S. E., Edwards, S., Cabrit, S., & Skrutskie, M. F. 1989, AJ, 97, 1451

Sumi, T., Kamiya, K., Bennett, D. P., et al. 2011, Nature, 473, 349

Sylvester, R. J., Skinner, C. J., Barlow, M. J., & Mannings, V. 1996, MN-RAS, 279, 915

Thi, W.-F., Pinte, C., Pantin, E., et al. 2014, A&A, 561, A50

van der Marel, N., Pinilla, P., Tobin, J., et al. 2015, ApJ, 810, L7

van Leeuwen, F. 2007, A&A, 474, 653

Wagner, K., Apai, D., Kasper, M., & Robberto, M. 2015, ApJ, 813, L2

Wahl, M., Metchev, S., Patel, R., et al. 2014, in IAU Symposium, Vol. 299, IAU Symposium, ed. M. Booth, B. C. Matthews, & J. R. Graham, 72

Walker, H. J., & Wolstencroft, R. D. 1988, PASP, 100, 1509

Watanabe, S.-i., & Lin, D. N. C. 2008, ApJ, 672, 1183

Weinberger, A. J., Becklin, E. E., Schneider, G., et al. 1999, ApJ, 525, L53

Weinberger, A. J., Rich, R. M., Becklin, E. E., Zuckerman, B., & Matthews, K. 2000, ApJ, 544, 937

Williams, J. P., & Cieza, L. A. 2011, ARA&A, 49, 67

Wisdom, J. 1980, AJ, 85, 1122

Woodgate, B. E., Kimble, R. A., Bowers, C. W., et al. 1998, PASP, 110, 1183

Wyatt, M. C. 2008, ARA&A, 46, 339

Zurlo, A., Vigan, A., Galicher, R., et al. 2015, ArXiv e-prints, 1511.04083

Appendix A

List of Publications

Refereed Papers

International

5. "The Matryoshka Disk: Keck/NIRC2 Discovery of a Solar System-scale,
   Radially Segregated Residual Protoplanetary Disk around HD 141569A"
   T. Currie, C. A. Grady, R. Cloutier, <u>M. Konishi</u>, K. Stassum, J. Debes,
   N. van der Marel, T. Muto, R. Jayawardhana, T. Ratzka
   submitted to Astrophysical Journal Letter

4. "Discovery of an Inner Disk Component around HD 141569 A"
   <u>M. Konishi</u>, C. A. Grady, G. Schneider, H. Shibai, M. W. McElwain,
   E. R. Nesvold, M. J. Kuchner, J. Carson, J. H. Debes, A. Gaspar,
   T. K. Henning, D. C. Hines, P. M. Hinz, H. Jang-Condell, A. Moro-
   Martín, M. Perrin, T. J. Rodigas, E. Serabyn, M. D. Silverstone, C. C. Stark,
   M. Tamura, A. J. Weinberger, J. P. Wisniewski
   accepted for Astrophysical Journal Letter
   arXiv: 1601.06560

3. "Indications of M-dwarf deficits in the halo and thick disk of the Galaxy"
   <u>M. Konishi</u>, H. Shibai, T. Sumi, M. Fukagawa, T. Matsuo, M. S. Sam-
   land, K. Yamamoto, J. Sudo, Y. Itoh, N. Arimoto, M. Kajisawa, L. Abe,
   W. Brandner, T. D. Brandt, J. Carson, T. Currie, S. E. Egner, M. Feldt,
   M. Goto, C. A. Grady, O. Guyon, J. Hashimoto, Y. Hayano, M. Hayashi,
   S. S. Hayashi, T. Henning, K. W. Hodapp, M. Ishii, M. Iye, M. Jan-
   son, R. Kandori, G. R. Kanapp, T. Kudo, N. Kusakabe, M. Kuzuhara,
   J. Kwon, M. W. McElwain, S. Miyama, J. Morino, A. Moro-Martín,
   T. Nishimura, T.-S. Pyo, E. Serabyn, T. Suenaga, H. Suto, R. Suzuki,
   Y. H. Takahashi, H. Takami, N. Takato, H. Terada, C. Thalmann,

D. Tomono, E. L. Turner, T. Usuda, M. Watanabe, J. P. Wisniewski,
T. Yamada, M. Tamura
Publication of the Astronomical Society of Japan, 67, 1, 2015
doi: 10.1093/pasj/psu125

2. "Far-Infrared Interferometric Telescope Experiment: Optical Adjustment System"
A. Sasaki, H. Shibai, M. Fukagawa, T. Sumi, T. Kanoh, K. Yamamoto,
Y. Itoh, N. Akiyama, A. Terano, Y. Aimi, Y. Kuwada, <u>M. Konishi</u>,
S. Sai, M. Narita
IEEE Transactions on Terahertz Science and Technology, vol. 4, 2, 179, 2014
doi: 10.1109/TTHZ.2013.2296996

1. "Direct Imaging Search of Extrasolar Planets in the Pleiades"
K. Yamamoto, T. Matsuo, H. Shibai, Y. Itoh, <u>M. Konishi</u>, J. Sudo,
R. Tani, M. Fukagawa, T. Sumi, T. Kudo, J. Hashimoto, N. Kusakabe,
L. Abe, W. Brandner, T. D. Brandt, J. Carson, T. Currie, S. E. Egner,
M. Feldt, M. Goto, C. Grady, O. Guyon, Y. Hayano, M. Hayashi,
S. Hayashi, T. Henning, K. Hodapp, M. Ishii, M. Iye, M. Janson,
R. Kandori, G. R. Knapp, M. Kuzuhara, J. Kwon, M. McElwain,
S. Miyama, J. Morino, A. Moro-Martín, J. Nishikawa, T. Nishimura,
T.-S. Pyo, E. Serabyn, H. Suto, R. Suzuki, M. Takami, N. Takato,
H. Terada, C. Thalmann, D. Tomono, E. L. Turner, J. Wisniewski,
M. Watanabe, T. Yamada, H. Takami, T. Usuda, M. Tamura
Publication of the Astronomical Society of Japan, 65, 90 (2013),
doi: 10.1093/pasj/65.4.90

Domestic (Japanese)

1. "太陽系外惑星検出に用いられる画像解析法の性能評価"
小西美穂子, 芝井 広, 松尾太郎, 山本広大, 住 貴宏, 深川美里
日本赤外線学会誌、Vol. 23, 1, p108, 2013

Conference Proceedings

International

2. "Estimation of Contaminants for Direct Imaging of Exoplanets: Constraint on the Stellar Distribution Model with both NIR and Deep

Imaging Data"
M. Konishi, H. Shibai, T. Matsuo, K. Yamamoto, J. Sudo, M. S. Samland, M. Fukagawa, T. Sumi
Proceedings of IAU, IAU Symposium, Vol. 299, 42, 2014

1. "Development of new optical adjustment system for FITE (Far-Infrared Interferometric Telescope Experiment)"
A. Sasaki, H. Shibai, T. Sumi, M. Fukagawa, T. Kanoh, K. Yamamoto, Y. Itoh, Y. Aimi, Y. Kuwada, Y. Kaneko, M. Konishi, S. Sai, N. Akiyama, M. Narita
Optical and Infrared Interferometry III. Proceedings of the SPIE, Volume 8445, article id. 84452Z, 9 pp., 2012

Appendix B

List of Presentations

Oral Presentations

International

2. "Indications of M-dwarf Deficits in the Halo and Thick Disk of the Galaxy"
<u>M. Konishi</u>, H. Shibai, T. Sumi, M. Fukagawa, T. Matsuo, M. S. Samland, K. Yamamoto, J. Sudo, Y. Itoh, N. Arimoto, M. Kajisawa, and SEEDS teams
SEEDS Workshop, Hyogo, Japan, October 2014

1. "Two ADI analysis algorism in the Random Noise area"
<u>M. Konishi</u>, T. Matsuo, H. Shibai, M. Fukagawa, K. Yamamoto, J. Sudo, Y. Itoh, R. Tanii
SEEDS Workshop, Kanagawa, Japan, October 2012

Domestic

11. "銀河系ハローと厚い円盤におけるM型星欠乏"
<u>小西美穂子</u>, 芝井 広, 住 貴宏, 深川美里, 松尾太郎, M. S. Samland, 山本広大, 須藤 淳, 伊藤洋一, 有本信雄, 鍛冶澤 賢, SEEDSチーム

10. "SEEDSによる散開星団での系外惑星探査5: 2013年度の進捗報告"
須藤 淳, 松尾太郎, 芝井 広, 住 貴宏, 深川美里, 山本広大, <u>小西美穂子</u>, M. S. Samland, 伊藤洋一, 田村元秀, HiCIAO/AO188/Subaruチーム
日本天文学会2014年秋季年会, P230a, 山形大学, 2014年9月

9. "FITE用圧縮型Ge:Ga二次元遠赤外線アレイの開発-II"
芝井 広, 秋山直輝, 中道みのり, 山本広大, 佐々木彩奈, 寺農 篤, 伊藤

哲史, 住 貴宏, 深川美里, 會見有香子, 桑田嘉大, 小西美穂子
日本天文学会2014年春季年会, W211a, 国際基督教大学, 2014年3月

8. "SEEDSによる散開星団での系外惑星探査4"
山本広大, 松尾太郎, 芝井 広, 住 貴宏, 深川美里, 小西美穂子, 須藤 淳,
M. S. Samland, 伊藤洋一, 田村元秀, HiCIAO/AO188/Subaruチーム
日本天文学会2013年秋季年会, P221a, 東北大学, 2013年9月

7. "SEEDS Direct Imaging Survey of Ursa Major Members"
M. S. Samland, T. Matsuo, H. Shibai, K. Yamamoto, M. Konishi,
J. Sudo, M. Fukagawa, T. Sumi, HiCIAO/AO188/Subaru Team
日本天文学会2013年秋季年会, P222a, 東北大学, 2013年9月

6. "太陽系外惑星探査における恒星混入率の導出：赤外線深撮像観測を
用いた銀河系恒星分布モデルへの制限"
小西美穂子, 芝井 広, 松尾太郎, 住 貴宏, 深川美里, 山本広大, 須
藤 淳, M. S. Samland, SEEDS/HiCIAO/AO188チーム
日本天文学会2013年秋季年会, P223a, 東北大学, 2013年9月

5. "気球搭載型遠赤外線干渉計FITE：次期フライト計画と高強度フレー
ムの開発"
芝井 広, 山本広大, 佐々木彩奈, 秋山直輝, 寺農 篤, 住 貴宏, 深川美
里, 會見有香子, 桑田嘉大, 小西美穂子, 成田正直, 吉田哲也, 斉藤芳
隆, 土居明広, 河野裕介
日本天文学会2013年秋季年会, W206a, 東北大学, 2013年9月

4. "直接撮像による系外惑星探査における二種類の解析方法の比較"
小西美穂子, 松尾太郎, 芝井 広, 深川美里, 山本広大, 須藤 淳, 伊藤洋
一, 谷井良子, SEEDS/HiCIAO/AO188チーム
日本天文学会2012年秋季年会, V222a, 大分大学, 2012年9月

3. "SEEDSによる散開星団での系外惑星探査3"
山本広大, 松尾太郎, 芝井 広, 深川美里, 小西美穂子, 須藤 淳, 伊藤洋
一, 谷井良子, 田村元秀, HiCIAO/AO188/Subaruチーム
日本天文学会2012年秋季年会, P203a, 大分大学, 2012年9月

2. "SEEDSによる散開星団での系外惑星探査2"
山本広大, 松尾太郎, 芝井 広, 深川美里, 小西美穂子, 伊藤洋一, 谷井
良子, 田村元秀, HiCIAO/AO188/Subaruチーム
日本天文学会2011年秋季年会, P67a, 鹿児島大学, 2011年9月

1. "SEEDSにおける系外惑星探査のための画像評価方法の開発"
小西美穂子, 松尾太郎, 芝井 広, 深川美里, 山本広大, 伊藤洋一, 谷井

良子, HiCIAO/AO188/Subaruチーム
日本天文学会2011年秋季年会, P68a, 鹿児島大学, 2011年9月

Poster Presentations

International

5. "Decoding Debris System Substructures: Imprints of Planets/Planetesimals and Signatures of Extrinsic Influences on Material in Ring-Like Disks"
C. A. Grady, G. Schneider, J. Carson, J. H. Debes, A. Gaspar, T. Henning, D. C. Hines, P. Hinz, H. Jang-Condell, M. J. Kuchner, A. Moro-Martin, M. D. Perrin, T. J. Rodigas, G. Serabyn, M. D. Silverstone, C. C. Stark, M. Tamura, A. J. Weinberger, J. P. Wisniewski, <u>M. Konishi</u>
American Astronomical Society 227th meeting, 343.10, Florida, USA, January 2016

4. "Deficit of M-dwarfs in the Halo and Thick Disk of the Galaxy: Estimation of the Number of Contaminating Stars for Direct Imaging Surveys"
<u>M. Konishi</u>, H. Shibai, T. Sumi, M. Fukagawa, T. Matsuo, K. Yamamoto, J. Sudo, M. S. Samland, Y. Itoh, N. Arimoto, M. Kajisawa, and the SEEDS teams
Origins 2014, Nara, Japan, July 2014

3. "Applying the M-dwarf Deficit Distribution Model of the Galaxy to Estimate the Number of Contaminants"
<u>M. Konishi</u>, H. Shibai, T. Sumi, M. Fukagawa, T. Matsuo, K. Yamamoto, J. Sudo, M. S. Samland, Y. Itoh, N. Arimoto, M. Kajisawa, and the SEEDS teams
2014 Sagan Exoplanet Summer Workshop, P38, California, USA, July 2014

2. "Direct Imaging Search for Extrasolar Giant Planets around 100 Myr-old Stars with Subaru Telescope"
<u>M. Konishi</u>, T. Matsuo, H. Shibai, K. Yamamoto, J. Sudo, M. S. Samland, M. Fukagawa, Y. Itoh, T. Sumi
The 5th Subaru International Conference, P36, Hawaii, USA, December 2013

1. "Deficit of M-dwarfs in the Halo and Thick Disk of the Galaxy"
<u>M. Konishi</u>, H. Shibai, T. Sumi, M. Fukagawa, T. Matsuo, K. Yamamoto, J. Sudo, M. S. Samland, Y. Itoh, N. Arimoto, M. Kajisawa

International Symposium on Research Frontiers of Physics, Earth and Space Science, No. 6, Osaka, Japan, December 2013

Domestic

9. "HD 141569 Aに付随する内円盤状成分の発見"
   小西美穂子, C. A. Grady, G. Schneider, 芝井 広, M. W. McElwain, E. R. Nesvold, M. J. Kuchner, 他 HST GO 13786 メンバー
   日本天文学会2016年春季年会（予定）, 首都大学東京、2016年3月

8. "FITE:スターカメラ用星像中心検出プログラムの高速化"
   伊藤哲史, 芝井 広, 佐々木彩奈, 中道みのり, 大山照平, 谷 貴人, 桑田嘉大, 小西美穂子, 須藤 淳, 住 貴宏, 山本広大, 成田正直
   日本天文学会2015年秋季年会, V229b, 甲南大学, 2015年9月

7. "気球搭載型遠赤外線干渉計 FITE:結像光学系の要求性能評価と公差解析"
   伊藤哲史, 芝井 広, 佐々木彩奈, 寺農 篤, 中道みのり, 住 貴宏, 深川美里, 桑田嘉大, 小西美穂子, 須藤 淳, 山本広大, 成田正直
   日本天文学会2014年秋季年会, W207b, 山形大学, 2014年9月

6. "遠赤外線干渉計 FITE:放物面鏡調整機構の開発"
   寺農 篤, 芝井 広, 佐々木彩奈, 伊藤哲史, 中道みのり, 住 貴宏, 深川美里, 桑田嘉大, 小西美穂子, 山本広大, 成田正直
   日本天文学会2014年秋季年会, W208b, 山形大学, 2014年9月

5. "遠赤外線干渉計FITEの新干渉計調整機構とその光学系の開発"
   佐々木彩奈, 芝井 広, 叶 哲生, 伊藤優佑, 山本広大, 秋山直輝, 住 貴宏, 深川美里, 會見有香子, 桑田嘉大, 小西美穂子, 成田正直
   日本天文学会2013年春季年会, W15c, 埼玉大学, 2013年3月

4. "遠赤外線干渉計FITE: 新長軽量平面鏡の開発"
   叶 哲生, 芝井 広, 伊藤優佑, 山本広大, 佐々木彩奈, 秋山直輝, 住 貴宏, 深川美里, 會見有香子, 桑田嘉大, 小西美穂子, 成田正直
   日本天文学会2013年春季年会, W16c, 埼玉大学, 2013年3月

3. "FITE用新放物面鏡調整機構の開発"
   片多修平, 秋山直輝, 芝井 広, 叶 哲生, 伊藤優佑, 山本広大, 佐々木彩奈, 住 貴宏, 深川美里, 會見有香子, 桑田嘉大, 小西美穂子, 成田正直
   日本天文学会2013年春季年会, W17c, 埼玉大学, 2013年3月

2. "FITE用遠赤外線圧縮型Ge:Ga二次元アレイセンサの開発"
   秋山直輝, 芝井 広, 伊藤優佑, 叶 哲生, 山本広大, 佐々木彩奈, 住 貴

宏, 深川美里, 會見有香子, 桑田嘉大, 小西美穂子, 成田正直
日本天文学会2013年春季年会, W18c, 埼玉大学, 2013年3月

2. "Two analysis methods for direct imaging of exoplanets"
小西美穂子, 松尾太郎, 芝井 広. 深川美里, 山本広大, 須藤 淳, 伊藤洋
一, 谷井良子
第8回太陽系外惑星大研究会, 静岡県, 2012年4月

1. "気球搭載型遠赤外線干渉計FITE：2010年実験結果と次期フライト計
画"
芝井 広, 住 貴宏, 深川美里, 叶 哲生, 幸山常仁, 伊藤優佑, 山本広大,
会見有香子, 金子有紀, 桑田嘉大, Dimitrios Kontopoulos, 小西美穂子,
蔡 承亨, 佐々木彩奈, 秋山直輝, 白井皓寅, 加藤恵理, 成田正直, 吉田
哲也, 斉藤芳隆, 下浦美那(IHI)、Antonio Mario Magalhaes, Jose William
Villas-Boas
日本天文学会2012年春季年会, W211c, 龍谷大学, 2012年3月

1. "New Destriping Method and the Detection Limit for Planets around
HD 23863"
小西美穂子, 松尾太郎, 芝井 広. 深川美里, 山本広大, 下浦美那, 会見
有香子, 伊藤洋一, 谷井良子
第7回太陽系外惑星大研究会, 東京都, 2011年3月